



# 1 Instant and delayed effects of march biomass burning aerosols over 2 the Indochina Peninsula

3 Anbao Zhu<sup>1,2</sup>, Haiming Xu<sup>1,2</sup>, Jiechun Deng<sup>1,2</sup>, Jing Ma<sup>1,2</sup>, Shaofeng Hua<sup>3</sup>

4 <sup>1</sup> Key Laboratory of Meteorological Disaster/KLME/ILCEC/CIC-FEMD, Nanjing University of Information Science &  
5 Technology, Nanjing 210044, China

6 <sup>2</sup>School of Atmospheric Sciences, Nanjing University of Information Science & Technology, Nanjing 210044, China

7 <sup>3</sup>CMA Weather Modification Centre (WMC), Beijing 100081, China

8 *Correspondence to:* Haiming Xu (hxu@nuist.edu.cn)

9 **Abstract.** Through analyzing observations and simulations from the Weather Research and Forecasting model coupled with  
10 Chemistry, we investigated instant and delayed responses of large-scale atmospheric circulations and precipitation to  
11 biomass burning (BB) aerosols over the Indochina Peninsula (ICP) in the peak emission of March. The results show that the  
12 BB aerosols inhibit precipitation over the ICP in March, and promote precipitation from early-April to mid-April.  
13 Specifically, the March BB aerosols over the ICP can induce mid-to-lower tropospheric heating and planetary boundary  
14 layer cooling, to enhance local atmospheric stability; meanwhile, the perturbation heating can trigger an anomalous low in  
15 the lower troposphere to moisten the mid troposphere. However, the convection suppression due to the stabilized atmosphere  
16 dominates over the favorable water-vapor condition induced by large-scale circulation responses, leading to an overall  
17 reduced precipitation over the ICP in March. For the delayed effect, the anomalous low can provide more water vapor as the  
18 monsoon advances in early-April, although it becomes much weaker without BB aerosols' strong heating. On the other hand,  
19 the convective instability above 850 hPa is enhanced by more water vapor, resulting in enhanced precipitation over the ICP,  
20 northern South China Sea, and southern China. Thereafter, the condensational latent heating gradually takes over from the  
21 BB aerosol radiative heating, acting as the main driver for maintaining the anomalous circulation and thus the delayed effect  
22 in mid-April.

## 23 1 Introduction

24 Biomass burning (BB), including agro-residue burning and forest or prairie fires, is one of the largest sources of many trace  
25 gases and aerosol particles in the atmosphere (Reid et al., 2005). Globally, BB contributes 42% of the black carbon (BC)  
26 emissions and 74% of the organic carbon (OC) emissions (Bond et al., 2004). Smoke aerosols produced by BB can reduce  
27 air quality, diminish visibility and harm public health (Huang et al., 2013; Yadav et al., 2017; Requia et al., 2021). BB-  
28 emitted aerosols also have vital impacts on regional climate and hydrological cycle through interactions with radiation,  
29 clouds and precipitation (Koren et al., 2004; Jacobson, 2014; Hodnebrog et al., 2016; Liu et al., 2020). The Indochina  
30 Peninsula (ICP) is one of the most active fire hotspots in the world (Lin et al., 2009; Gautam et al., 2013; Yadav et al., 2017),



with high population density, thus high social and economic relevance, and with strong monsoon circulation variability (Li et al., 2016; Wu et al., 2016). Therefore, it is essential to investigate the feedback mechanisms of BB aerosols-climate interactions to better understand aerosols' climatic and socio-economic impacts (Lau, 2016; Ding et al., 2021).

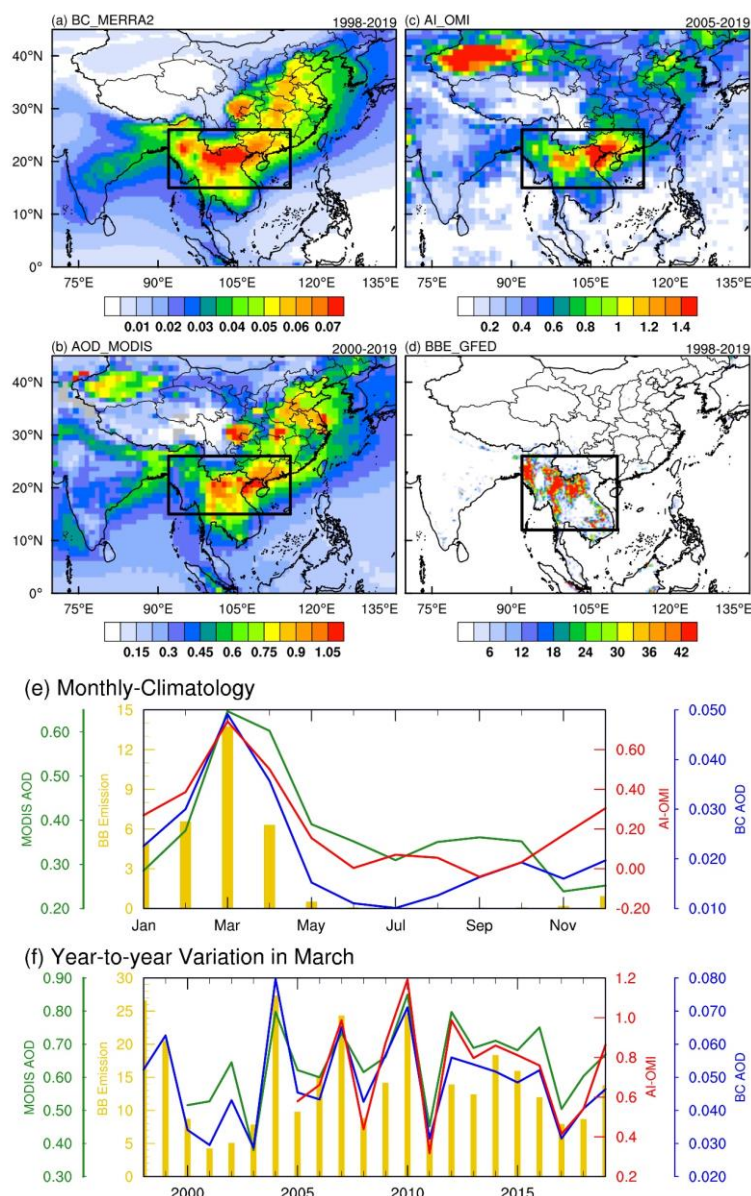
BB aerosols can affect the climate in several ways. The aerosols, such as BC and OC aerosols, can directly scatter and absorb solar radiation (i.e., the so-called “direct effect”), thereby reducing the solar radiation reaching the surface. Both observational and numerical studies suggested that BB aerosols' direct effect can inhibit vertical instability by heating the atmosphere of the smoke aerosol layer and cooling the surface, thereby reducing surface fluxes and suppressing warm-cloud formation and convective activity (Koren et al., 2004; Feingold et al., 2005; Hodnebrog et al., 2016; Huang et al., 2016b), and enhancing low-cloud fraction (Sakaeda et al., 2011; Lu et al., 2018; Ding et al., 2021). On the other hand, BB aerosols can locally reduce precipitation by serving as cloud condensation nuclei and ice nuclei, increasing cloud droplet number concentration, decreasing droplet effective radii (i.e., “indirect effect”), and decelerating the autoconversion process (Lee et al., 2014; Liu et al., 2020; Herbert et al., 2021). Numerical modelling studies have found that the direct effect dominates at low BB aerosol loading, while the indirect effect dominates at high BB aerosol loading (Liu et al., 2020; Herbert et al., 2021). However, the initial suppressive effect of BB aerosols on rainfall can lead to convective invigoration by cold rain processes (Martins et al., 2009). BB aerosols may also enhance rainfall under certain conditions, which are highly dependent on factors such as the altitude and longevity of the smoke plume (Tummon et al., 2010; Ban-Weiss et al., 2012; Herbert et al., 2021), the atmospheric degree of instability (Gonçalves et al., 2015) and the diurnal cycle of the convective system (Lee and Wang, 2020; Herbert et al., 2021). The above-mentioned perturbations caused by BB aerosols can also affect large-scale atmospheric circulation, thus changing the regional climate (Zhang et al., 2009; Lee et al., 2014; Jiang et al., 2020; Zhou et al., 2021).

The ICP experiences substantial agro-residue burning across farmlands in preparation for planting during the dry season, typically between February and April with a maximum occurrence in March (Huang et al., 2013; Shi et al., 2014) (Figs. 1a–e). Large amounts of BB aerosols are injected into the atmosphere, uplifted up to 3-km height by the India-Burma trough and transported to southern China and the South China Sea (SCS), and even to the western North Pacific Ocean by the subtropical southwesterly jet (Lin et al., 2009; Huang et al., 2013; Huang et al., 2016a; Zhu et al., 2021). The BB aerosols become minimal after the monsoon rainfall onset in late-April due to rainout and washout processes (Huang et al., 2016a).

The effects of BB aerosols over the ICP on regional air quality (Lin et al., 2009; Huang et al., 2013; Lin et al., 2014; Yang et al., 2022a) and climate (Lee and Kim, 2010; Lee et al., 2014; Pani et al., 2018; Dong et al., 2019; Wang et al., 2021; Yang et al., 2022b) have been widely investigated based on observations and numerical modeling studies. However, aerosol-cloud-precipitation interactions over the ICP have rarely been explored. Using an atmospheric global climate model (AGCM) coupled with an aerosol module, Lee and Kim (2010) showed that BC's radiative forcing (including anthropogenic and BB-emitted) in East Asia induces an anomalous meridional circulation through radiation effect during spring. The anomalous upward motion near 30°N causes increased precipitation over Myanmar and Bangladesh, while the anomalous downward motion around 10°N causes a decrease in precipitation over Southeast Asia. Based on the Goddard Earth Observing System



65 version 5 (GEOS-5)/AGCM model, Lee et al. (2014) suggested that both the direct effect (increasing lower-atmospheric  
66 stability) and indirect effect (decelerating cloud droplet autoconversion process) of BB aerosols can suppress local  
67 precipitation in the ICP during the pre-monsoon season (March–April), and the large-scale advection of cloud moisture  
68 invigorates the downwind rainfall. Yang et al. (2022b) utilized the Weather Research and Forecasting model coupled with  
69 Chemistry (WRF-Chem) to show that the increased atmospheric stability induced by BB aerosols inhibits local rainfall over  
70 the ICP. The low-level cyclonic anomaly wind induced by the BB aerosol heating can modify moisture transport, leading to  
71 increased (decreased) rainfall over the southern coast (northern inland) of southern China. A case study by Wang et al. (2021)  
72 revealed that BB aerosols transported from the ICP can suppress convective precipitation and enhance non-convective  
73 precipitation over southern China. Most of these studies focused on the seasonal time scale (Lee and Kim, 2010; Lee et al.,  
74 2014; Yang et al., 2022b) or individual cases lasting a few days (Wang et al., 2021). However, the BB emission over the ICP  
75 has a strong intra-seasonal variability peaking in March (Fig. 1e), whose instant and delayed effects on the climate remain  
76 unclear.



77

78 **Figure 1: Spatial distribution of March (a) black carbon (BC) aerosol optical depth (AOD; shading, unitless) averaged over 1998–**  
 79 **2019 from MERRA-2, (b) AOD (unitless) averaged over 2000–2019 from MODIS Terra, (c) aerosol index (AI; unitless) averaged**  
 80 **over 2005–2019 from OMI, and (d) biomass burning (BB) carbon emission (shading;  $\text{g C m}^{-2} \text{ month}^{-1}$ ) averaged over 1998–2019**  
 81 **from GFEDv4.1. (e) Monthly climatology of BB aerosol indices (blue line for BC AOD, green line for AOD, red line for AI) and**  
 82 **emission (gold bar) averaged over Indochina [ $92^{\circ}\text{--}115^{\circ}\text{E}$ ,  $15^{\circ}\text{--}26^{\circ}\text{N}$  for BC AOD, AOD and AI;  $92^{\circ}\text{--}110^{\circ}\text{E}$ ,  $12^{\circ}\text{--}26^{\circ}\text{N}$  for BB**  
 83 **emission; as outlined by the black boxes in (a–d)]. (f) Same as (e), but for the time series of monthly averaged BB aerosol indices in**  
 84 **March.**

85 In this study, we examine the impacts of March BB aerosols over the ICP using both observations and model experiments. In  
 86 particular, we address the following questions: (1) What are the instant and delayed effects of March BB aerosols over the  
 87 ICP on atmospheric circulation and precipitation? (2) What are the differences between these two effects and what are their



underlying physical mechanisms? The remaining paper is organized as follows. In Sect. 2, we describe the data, methods, model, and experimental design. In Sect. 3, we present the observed evidence of BB aerosol impacts on circulation and precipitation. In Sect. 4, we discuss the responsible physical mechanisms based on simulation results. Conclusions and discussion are provided in Sect. 5.

## 2 Methodology

### 2.1 Data and statistical methods

The meteorological and BC aerosol data used in this study are the Modern Era Retrospective analysis for Research and Applications Version 2 (MERRA-2) from the National Aeronautics and Space Administration (NASA) Global Modeling and Assimilation Office (GMAO) (Gelaro et al., 2017), with a spatial resolution of  $0.5^\circ$  by  $0.65^\circ$  (longitude by latitude) on 72 levels. MERRA-2 reanalysis is the first satellite era (1980 onward) reanalysis data jointly assimilating meteorological and aerosol observations. The MERRA-2 aerosol data is produced using the Goddard Chemistry Aerosol Radiation and Transport (GOCART) aerosol model coupled to the GEOS-5 data assimilation system. The GOCART model simulates five aerosol species: dust, black carbon, organic carbon, sulfate and sea salt. The GEOS-5 assimilates the bias-corrected aerosol optical depth (AOD) from the Advanced Very High Resolution Radiometer (AVHRR) instrument over the ocean (Heidinger et al., 2014), the Moderate resolution Imaging Spectroradiometer (MODIS) from the Terra and Aqua satellites (Levy et al., 2010), Multiangle Imaging SpectroRadiometer (MISR) AOD over land (Kahn et al., 2005), and ground-based Aerosol Robotic Network (AERONET) AOD (Holben et al., 1998). Numerous evaluations on the MERRA-2 aerosol data have shown that both the AOD and the vertical structure of aerosol properties in the MERRA-2 have good agreement with the observations (Buchard et al., 2017). In this study, we use the monthly mean BC AOD.

We also use the AOD from 1° MODIS Terra Level-3 monthly product (MOD08\_M3) (Gupta et al., 2016), aerosol index (AI) from 1° Ozone Monitoring Instrument (OMI)/Aura Level-3 daily product (OMAERUVd) (Torres et al., 2007) and BB emissions from the Global Fire Emissions Database version 4.1 (GFEDv4) (Randerson et al., 2017) to compare with MERRA-2 BC AOD. In addition, we use the atmospheric fields from the fifth generation European Centre for Medium-Range Weather Forecasts (ECMWF) reanalysis data (ERA5) (Hersbach and Dee, 2016), including zonal and meridional wind components on  $0.25^\circ$  grid. The monthly and daily precipitation data on  $0.25^\circ$  grid is from the Tropical Rainfall Measuring Mission (TRMM) Multi-satellite Precipitation Analysis (TMPA) 3B43 and 3B42 (Huffman et al., 2007), respectively.

For consistency, the precipitation data from the TRMM, the ERA5 reanalysis data, the GFEDv4 BB emissions, and MERRA-2 BC AOD all cover the same period of 1998–2019. MODIS AOD and OMI AI cover the periods of 2000–2019 and 2005–2019, respectively. In this study, we focus on the effect of March BB aerosols on regional climate in early-spring (March 1<sup>st</sup>–April 20<sup>th</sup>), including the instant effect in March and the delayed effect in early-April (1<sup>st</sup>–10<sup>th</sup>) and mid-April (11<sup>th</sup>–20<sup>th</sup>). The linear-regression analysis is used and subjected to the two-tailed Student's *t*-test for statistical significance.





## 2.1 Model and experimental design

In this study, the WRF-Chem version 4.2.1 is used to simulate the evolution of BB aerosols and trace gases, to investigate their interactions with meteorological conditions over the ICP and East Asia. The model is configured to cover the Bay of Bengal, ICP and East Asia (Fig. 2) with  $331 \times 255$  grids at 27-km horizontal resolution and 42 levels from the ground to 50 hPa. The planetary boundary layer (PBL) processes are parameterized using the Mellor-Yamada-Janjic (MYJ) scheme with local vertical mixing (Janjić, 1994), combined with the Noah Land Surface Model and the Monin-Obukhov scheme for the surface layer physical processes and the interaction with land surface (Chen et al., 2010; Pahlow et al., 2001). The Rapid Radiative Transfer Model for General circulation models (RRTMG) coupled with aerosol radiative effect is used for both shortwave (SW) and longwave (LW) radiation (Iacono et al., 2008). The double-moment Morrison microphysics scheme (Morrison et al., 2009) and Grell-Freitas (GF) cumulus scheme (Grell and Freitas, 2014) are used to ensure that aerosol indirect effects are included. The Carbon-Bond Mechanism version Z (CBMZ) gas-phase chemistry mechanism combined with the Model for Simulating Aerosol Interactions and Chemistry (MOSAIC) aerosol module (Zaveri and Peters, 1999; Zaveri et al., 2008) are selected for aerosol simulation. Aerosol optical properties are calculated based on the Maxwell approximation (Bohren and Huffman, 1983).

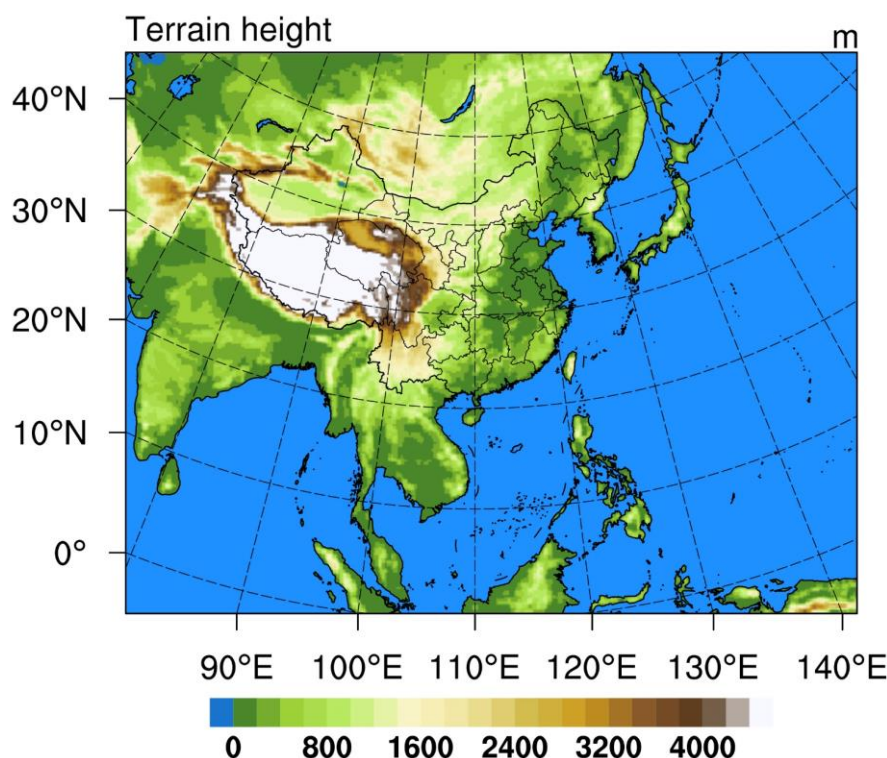


**Figure 2: Model domain and orography (shading; m).**

The boundary and initial conditions of meteorological fields are derived from the National Centers for Environmental Prediction (NCEP) Final Analysis (FNL) data with  $1^\circ$  spatial resolution and 6-h temporal interval. The input sea-surface



temperature (SST) data is the NCEP real time global SST analysis. The anthropogenic emission source comes from the Multi-resolution Emission Inventory for China (MEIC) database for China (Li et al., 2017a) and from the MIX inventory (Li et al., 2017b) for regions outside of China. The biogenic emissions are calculated online using the Model of Emissions of Gases and Aerosols from Nature (MEGAN) (Guenther et al., 2012). The GOCART dust emission scheme with the Air Force Weather Agency (AFWA) modifications (LeGrand et al., 2019) is used to simulate dust emissions. The high-resolution fire emissions based on the Fire INventory from NCAR (FINN) version 1.5 (Wiedinmyer et al., 2011) are selected as the BB emissions. Specific settings are listed in Table 1.

**Table 1. WRF-Chem model parameterization option settings and emissions used in this study**

Option name	Scheme
Longwave radiation	RRTMG
Shortwave radiation	RRTMG
Microphysics	Morrison 2-mom
Boundary layer	MYJ
Cumulus	Grell-Freitas
Land surface	Unified Noah
Surface layer	MM5 Monin-Obukhov
Aerosol chemistry	MOSAIC
Gas chemistry	CBMZ
Photolysis	Fast-J
Aerosol mixing rule	Maxwell–Garnett approximation
Dust emissions	GOCART-AFWA
Biogenic emissions	MEGAN version 2
Anthropogenic emissions	MEIC for China and MIX for outside of China
Biomass burning emissions	FINN version 1.5

To investigate the impacts of March BB aerosols on radiation, circulation and precipitation, we conduct two groups of simulations with different BB emission scenarios and compare these results. The control experiment (CTRL) has the original BB emissions, while the sensitivity experiment (BBER) has the March BB emissions reduced to 15%. To increase the robustness of our findings, we use six ensemble members for each experiment by perturbing initial and boundary conditions, that is, the ensemble simulations start at one day apart on February 20<sup>th</sup>–25<sup>th</sup>, 2010, respectively, and all end on April 30<sup>th</sup>, 2010. Thus, different starting day in February for each member is discarded as spin-up time, and we only focus on the period from March 1<sup>st</sup> to April 20<sup>th</sup>, 2010. We chose the year of 2010 for modeling because the BB emission in 2010 was above the



average and was about six times higher than that in 2001 (the lowest year during 1998–2019 and similar to the BB reduction used in BBER; Fig. 1f), which is suitable for investigating the effects of BB aerosols on atmospheric circulation and precipitation.

### 3 Observations

#### 3.1 Variation in BB aerosols

For observational evidence of possible responses of atmospheric circulation and precipitation to BB aerosols, we first examine the spatial distribution of the climatological mean BB aerosols in March (Figs. 1a–d) and their temporal variation (Fig. 1f) via multiple data sources. The spatial pattern of BB aerosols from the aerosol reanalysis data (MERRA-2) is quite consistent with multiple satellite retrievals (Figs. 1a–d). The high BC aerosol loading is concentrated in the northern ICP with a maximum BC AOD exceeding 0.07 (Fig. 1a), which is contributed by BB emissions (Fig. 1d). High BC AOD also appears over the Sichuan Basin and central-eastern China, likely caused by anthropogenic activities (Qin and Xie, 2012; Ning et al., 2018). High MODIS AOD values are also seen over northwestern China (Fig. 1b), as large dust aerosols are emitted from the Taklimakan Desert in March (Bao et al., 2009). As positive AI generally represents absorbing aerosols (dust and smoke), high AI is found over the northern ICP and northwestern China (Fig. 1c). Unlike the high BC loading over the Sichuan Basin and central-eastern China (Fig. 1a), the AI is small over these regions likely because the AI's sensitivity to aerosol amount increase more or less proportionally with the aerosol layer height, while any aerosol below about 1000 m is unlikely to be detected (de Graaf et al., 2005). The dust and BB aerosols are transported eastward at higher atmospheric levels and are more easily detected, whereas anthropogenic pollution transport mainly occurs within the boundary layer, giving rise to smaller AI (Kaskaoutis et al., 2010).

For temporal variation, the BC AOD from the MERRA-2 over the ICP agrees well with satellite datasets and BB emissions. Figure 1f shows the time series of area-averaged monthly BB aerosol indices in March for the northern ICP ( $92^{\circ}$ – $115^{\circ}$  E,  $15^{\circ}$ – $26^{\circ}$  N for BC AOD, AOD and AI;  $92^{\circ}$ – $110^{\circ}$  E,  $12^{\circ}$ – $26^{\circ}$  N for BB emissions). The correlations between the time series of MERRA-2 BC AOD and MODIS AOD (2000–2019), AI (2005–2019), and BB emission (1998–2019) are 0.90, 0.93 and 0.85, respectively; all are statistically significant at the 99 % level. This indicates that the BB aerosols over the ICP have large interannual fluctuation in March, consistent with the recent study by Ding et al. (2021) based on multiple satellite records. However, such interannual variation could be influenced by meteorological factors such as the India-Burma trough (Huang et al., 2016a) and El Niño–Southern Oscillation (ENSO) (Zhu et al., 2021). On the other hand, the interannual fluctuation can be used to detect climate effects of the aerosols. Given this, we define a BB aerosol index (BBAI) the time series of MERRA-2 BC AOD (1998–2019, blue line in Fig. 1f) to explore BB aerosols' effects on atmospheric circulation and precipitation.





### 3.2 Relationship between BB aerosols and precipitation

Figure 3 shows the regressed anomalies of BC AOD, precipitation and 850-hPa wind upon the BBAI in March and in early-to-mid April. In March, significant positive BC AOD anomalies are seen over the ICP, northern SCS, southern China, and the ocean south of Japan (Fig. 3a), as the BB aerosols emitted from the central and northern ICP are transported eastward by the prevailing winds (Lin et al., 2009; Huang et al., 2013; Huang et al., 2016a; Huang et al., 2020). Correspondingly, the rainfall over the ICP is reduced by anomalous westerly wind, while the rainfall in coastal Southeast China is enhanced by anomalous southerly wind (Fig. 3d), forming a dipole anomaly structure.

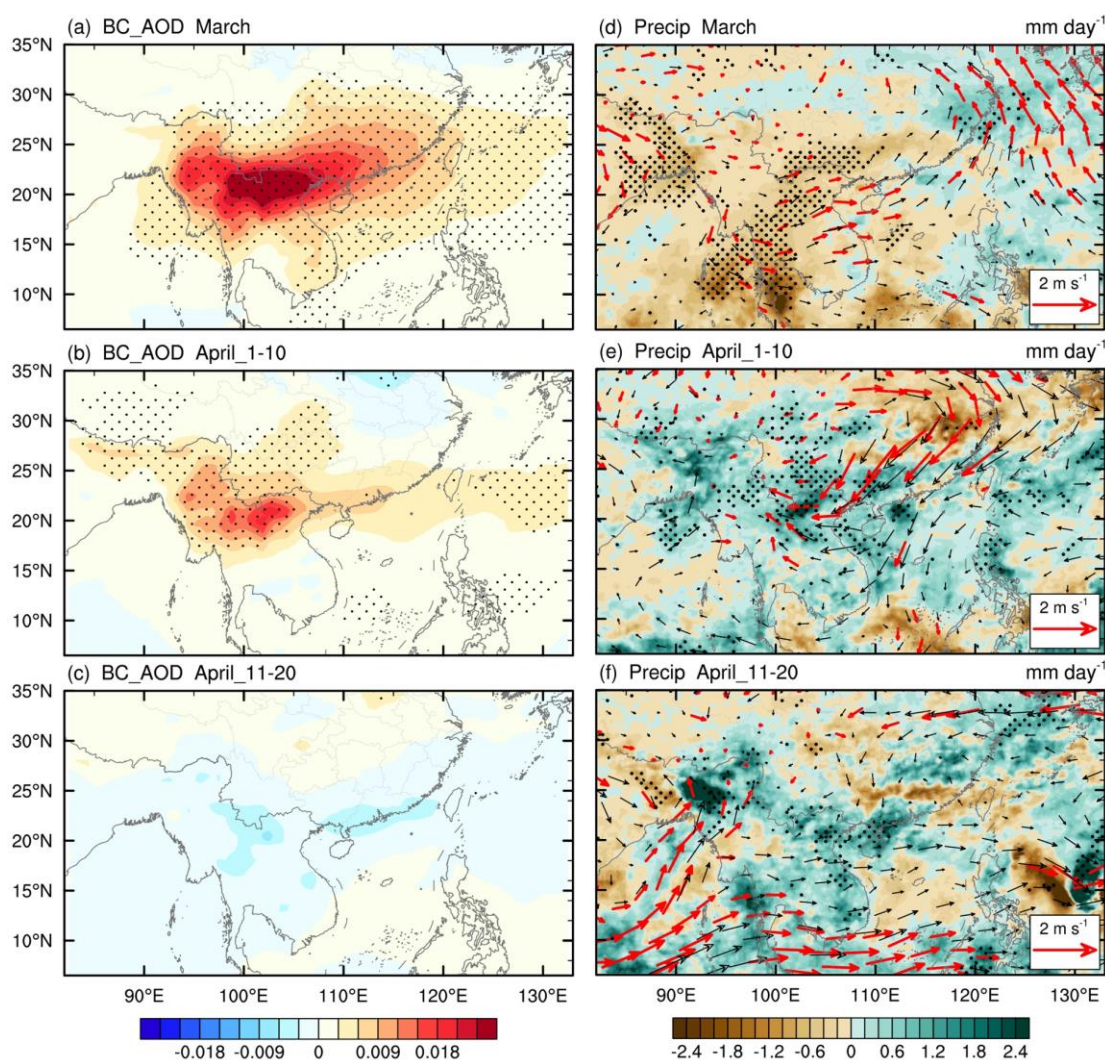


**Figure 3:** Regressions of anomalies in (a–c) BC AOD (shading; unitless) and in (d–f) precipitation (shading;  $\text{mm day}^{-1}$ ) and 850-hPa wind (vector;  $\text{m s}^{-1}$ ) onto standardized BBAI in (a, d) March, and in (b, e) early-April and (c, f) mid-April. Stippling (red vector) denotes the regressed anomalies of BC AOD and precipitation (of wind) are statistically significant at the 95% confidence level based on Student's *t*-test.



196 Generally, the lifetime of BB aerosols and their eastward transport life cycle last a few days to weeks (Deng et al., 2008;  
197 Huang et al., 2020; Adam et al., 2021). Thus, significant positive BC AOD anomalies are still observed over the northern  
198 ICP, southwestern China and the Northwest Pacific east of Taiwan in early-April (Fig. 3b). However, the precipitation  
199 anomaly pattern is roughly opposite to that in March, with above-normal precipitation from the northern Bay of Bengal  
200 eastward to the northern SCS and below-normal precipitation over the middle and lower reaches of the Yangtze River (Fig.  
201 3e). Correspondingly, significant anomalous northeasterly wind occurs from the middle and lower reaches of the Yangtze  
202 River toward the northern ICP, acting to reduce the climatological south-westerly wind and the water-vapor transport in  
203 southern China. When mid-April comes, no significant BB aerosol anomalies can be found (Fig. 3c), but the positive  
204 precipitation anomalies still exist over the northern and eastern ICP and the Beibu Gulf, accompanied by anomalous westerly  
205 wind across the Indo-Pacific Ocean and southwesterly wind from the northern tropical Indian Ocean to the northwestern ICP  
206 (Fig. 3f). As no significant anomalies are found in circulation and precipitation after about April 20<sup>th</sup>, we will focus on the  
207 features in early- to mid-April.

208 As mentioned above, the March BB aerosols can reduce precipitation over the ICP in March but increase precipitation from  
209 April 1<sup>st</sup> to around April 20<sup>th</sup>, indicating that the effects of March BB aerosols on precipitation can last from March to early-  
210 to-mid April, but with opposite effects in the two months. Due to the covariation of aerosols and meteorological fields, it is  
211 hard to determine the causality between BB aerosols over the ICP and atmospheric circulation (and precipitation), especially  
212 using instant observations. Therefore, in the following section, we will use two groups of WRF-Chem experiments to reveal  
213 the physical mechanisms responsible for these relationships.

## 214 **4 Numerical modeling results**

### 215 **4.1 Evaluation of model results**

216 Figures 4a–b illustrate the spatial patterns of the observed and modelled rainfall and 850-hPa wind averaged from March 1<sup>st</sup>  
217 to April 20<sup>th</sup>, 2010. The TRMM data shows a large rainfall belt extending from the Nanling Mountains to the south of the  
218 Yangtze River (110°–120°E, 23°–30°N) (Fig. 4a), known as spring persistent rainfall in Jiangnan of China (SPRJ). (Note:  
219 Jiangnan is the name in Chinese for the region south of the Yangtze River). In addition, large amounts of precipitation can  
220 also be found over the northwestern ICP region, which is typical orographic precipitation on the windward side of the slope.  
221 The WRF-Chem ensemble-mean rainfall based on six CTRL members (Fig. 4b) shows a spatial pattern consistent with that  
222 in the TRMM, although the model overestimates the convection in the northern tropical Indian Ocean, orographic  
223 precipitation in the northwestern ICP region, and rainfall south of Japan. Similar overestimate tropical convection and  
224 orographic precipitation can be seen in Yang et al. (2022b) using the same model. The atmospheric circulation in East Asia  
225 during early-spring (March 1<sup>st</sup>–April 20<sup>th</sup>) 2010 is featured by strong easterly winds across the tropical Indo-Pacific Ocean  
226 and southwesterly winds from the Bay of Bengal and SCS to southern China (Fig. 4a). In general, the model can reasonably  
227 capture these observed features of rainfall and circulation.

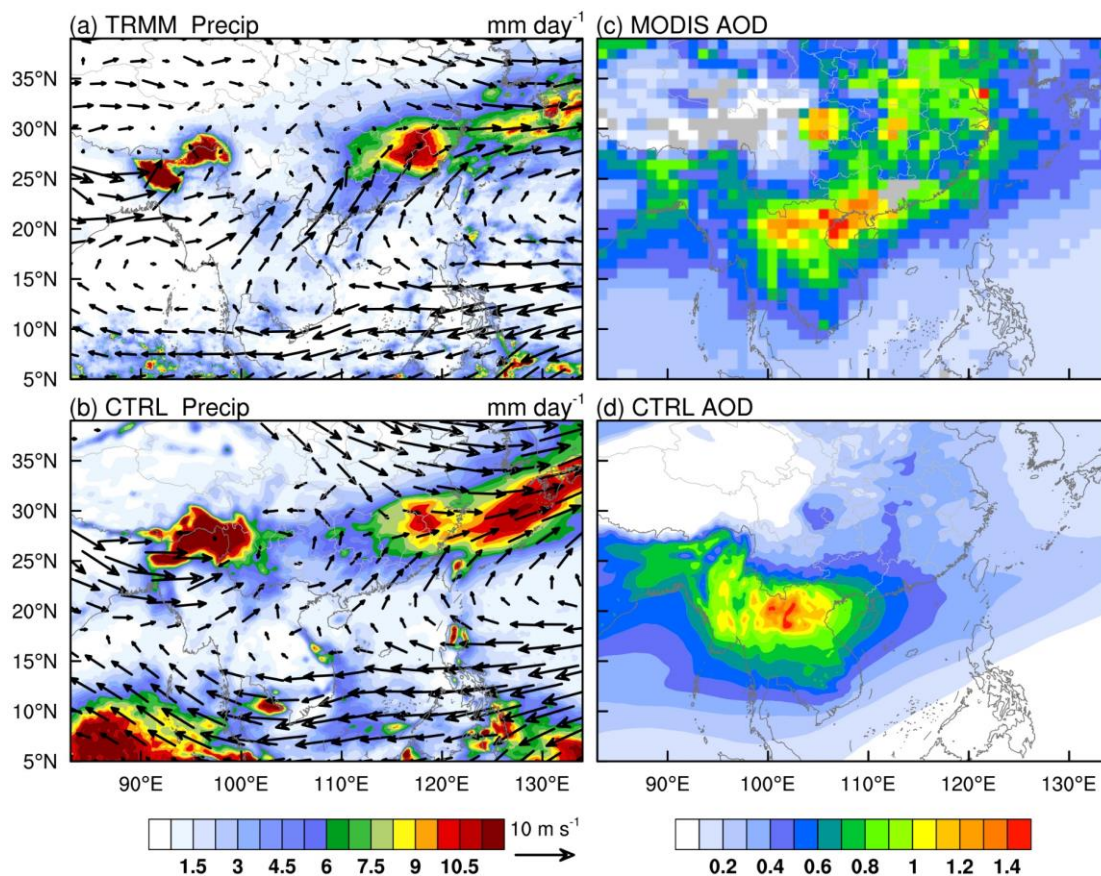


**Figure 4:** Spatial distributions of precipitation (shading; mm day<sup>-1</sup>) and 850-hPa wind (vector; m s<sup>-1</sup>) averaged over early spring (March 1<sup>st</sup> to April 20<sup>th</sup>) of 2010 from (a) observations (TRMM precipitation and ERA-5 wind) and (b) ensemble-mean of WRF-Chem CTRL. (c, d) Same as (a, b), but for AOD (shading; unitless) from (c) MODIS and (d) ensemble-mean of WRF-Chem CTRL.

The spatial pattern of modeled AOD is consistent with MODIS satellite retrieval. Figures 4c–d show that the WRF-Chem can capture the observed high aerosol loading over the ICP; however, it underestimates the AOD over eastern China and its coastal regions. The differences between model simulations and satellite data could be attributed to two potential factors. First, the WRF-Chem model does not fully cover the effect of relative humidity on AOD calculation, as increased relative humidity can lead to higher AOD because of aerosol humidification (Myhre et al., 2007). Second, the GOCART AFWA scheme can underestimate the dust aerosol concentration in northwestern China (Zhao et al., 2020), resulting in a lower AOD in northern China. Nevertheless, the WRF-Chem model has a good performance in simulating the BB aerosols over the ICP.

Given this, the ensemble-mean differences between CTRL and BBER (i.e. CTRL minus BBER) are used to examine the effects of BB aerosols and associated physical mechanisms.





## 243 4.2 Effects of BB aerosols

244 Figure 5 shows the BB aerosol-induced differences in AOD, rainfall and 850-hPa wind during March and early-to-mid April  
245 of 2010. The BB aerosols significantly increased in March due to BB emissions, with a maximum AOD anomaly exceeding  
246 1.2 over the northern ICP (Fig. 5a). The AOD anomaly pattern of AOD agrees well with observations (Fig. 3a). The BB  
247 aerosol-induced anomalous circulation exhibits a belt-shaped low-pressure band in the lower troposphere (850 hPa) over  
248 Southeast Asia, with two centers located to the east (Hainan Island) and west (coastal southern Myanmar) of the ICP (Fig.  
249 5d). Correspondingly, the precipitation decreased by roughly 13% from the northern Bay of Bengal to southern China. This  
250 was probably because the anomalous easterly wind on the northern flank of the low-pressure zone acted to weaken the  
251 prevailing southwesterly wind (Fig. 4b), thereby reducing the moisture transport from the Bay of Bengal and SCS. In  
252 addition, the precipitation was reduced by about 15% over most of the ICP (Fig. 5d), which was the emission source region.  
253 This might be related to the suppressive effect of BB aerosols on local convection (Hodnebrog et al., 2016; Yang et al.,  
254 2022b). The largest rainfall reduction occurred in the northwestern ICP, with a maximum exceeding 2 mm day<sup>-1</sup>. The BB  
255 aerosol-induced rainfall reduction over the emission source region is consistent with observations (Fig. 3d). Enhanced  
256 precipitation occurred in the western and northern SCS, East China Sea, and their coastal regions, under southerly wind  
257 anomalies. These simulated changes in rainfall and circulation induced by March BB aerosols agree well with the results  
258 based on climate models (Lee et al., 2014; Chavan et al., 2021) and mesoscale weather models (Wang et al., 2021; Yang et  
259 al., 2022b).

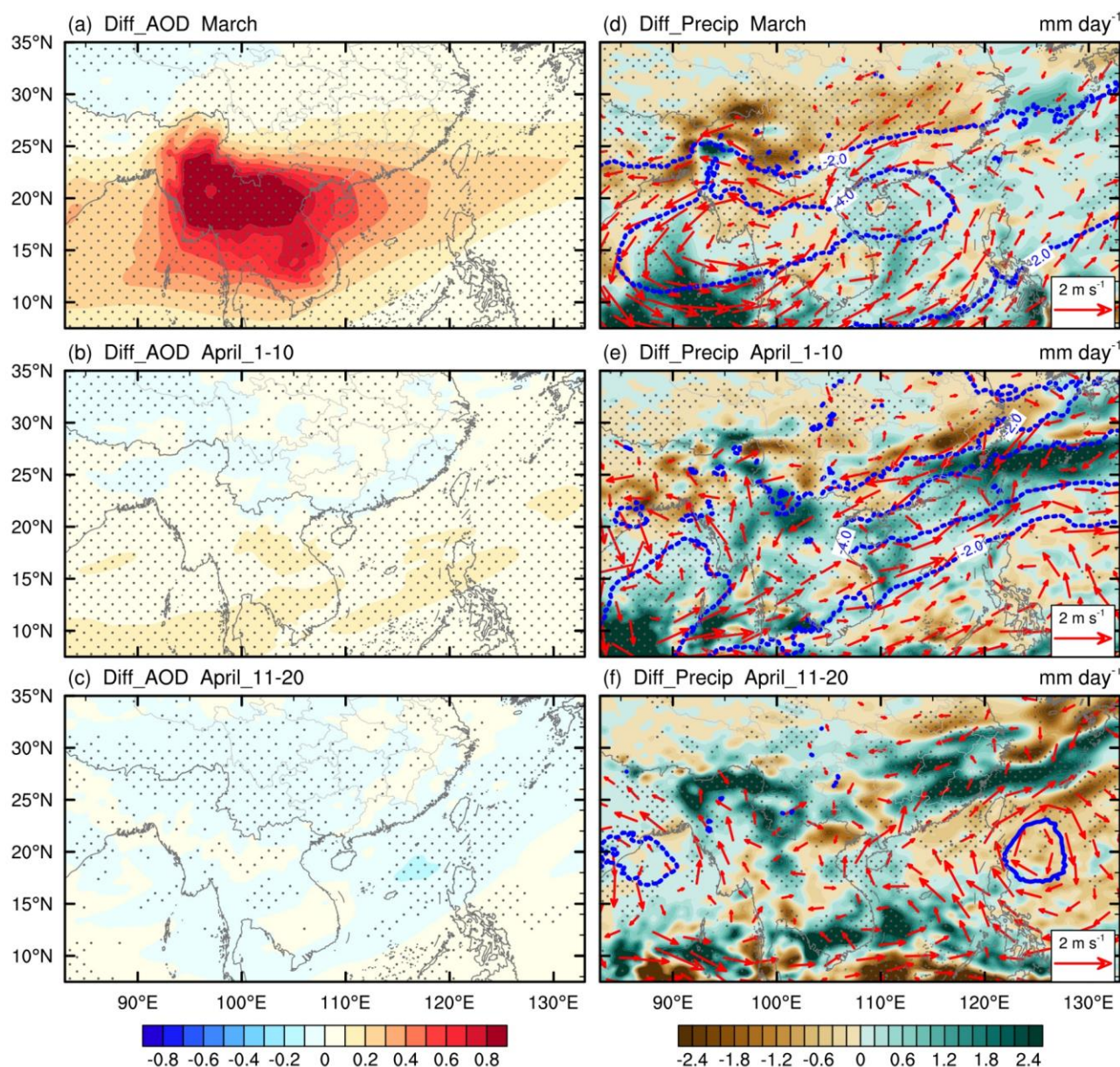


**Figure 5:** WRF-Chem-simulated ensemble-mean differences in (a–c) AOD (shading; unitless) and (d–f) precipitation (shading; mm day<sup>-1</sup>), 850-hPa wind (vector; m s<sup>-1</sup>) and geopotential height (blue contours with interval of 2 dagpm; the dashed contours are for negative values and the zero contour is omitted for clarity) between CTRL and BBER (i.e., CTRL minus BBER) during (a, d) March, (b, e) early-April and (c, f) mid-April of 2010. Stippling (red) denotes the AOD and precipitation (wind) are statistically significant at the 95% confidence level based on Student's *t*-test.

As in the observations (Fig. 3b), positive aerosols anomalies due to March BB emissions were still evident (albeit smaller) in early-April (Fig. 5b). The centers of the belt-shaped anomalous low at 850 hPa were located over coastal southern China and the southern Bay of Bengal (Fig. 5e). This indicates that the circulation response to March BB aerosols did not disappear immediately and could last from March to early-April, although it became weak. However, the precipitation promotion due





270 to March BB aerosols dominated over the entire ICP region in early-April, contrary to the rainfall reduction in March.  
271 Besides, the SPRJ rainband shifted markedly southward characterized by reduced precipitation in the middle and lower  
272 reaches of the Yangtze River and by increased precipitation from coastal Southeast China to the East China Sea. These  
273 responses of rainfall and circulation to March BB emissions are similar to those in observations shown in Sect. 3.2. Since  
274 aerosol concentration anomalies in April were affected a little by the March BB emissions, the anomalous rainfall in early-  
275 April could be potentially caused by the large-scale circulation change.

276 During mid-April, no significant AOD differences appeared over the ICP (Fig. 5c). The BB aerosol-induced belt-shaped  
277 850-hPa low-pressure band almost dissipated, with only small cyclonic anomaly wind in the northern Bay of Bengal (Fig. 5f).  
278 The anomalous southerly wind in the western ICP transported moisture from the Bay of Bengal to the northern ICP and  
279 increased precipitation in the northwestern IPC along the topography on the southeastern side of the Tibetan Plateau. Clearly,  
280 the observed circulation and precipitation anomalies in mid-April (Fig. 3f) can also be reproduced in the WRF-Chem model.

### 281 4.3 Physical mechanism underlying the BB aerosols-rainfall relationship

#### 282 4.3.1 Instant effect

283 The BB aerosols can significantly change radiative forcing by absorption and scattering of solar radiation, leading to spatial  
284 perturbation and redistribution of energy (Chavan et al., 2021). Figures 6a–c shows the BB aerosol-induced changes in net  
285 downward SW radiative fluxes at the top of the atmosphere (TOA), in the atmosphere, and at the surface under all-sky  
286 conditions in March. BB aerosols can absorb SW radiation and heat up the atmosphere. Thus, positive SW radiation  
287 anomalies dominate in the atmosphere over the regions with high BB aerosol loading, with a magnitude of 30–65 W m<sup>-2</sup>  
288 from the Bay of Bengal across the ICP to the coastal region of South China and the SCS (Fig. 6b). At the surface, BB  
289 aerosols prevent the solar radiation from reaching the surface by scattering and absorption, which causes a surface cooling  
290 effect over the high BB aerosol loading regions, as shown in Fig. 6c. The maximum magnitude of the negative SW radiative  
291 flux anomalies is about 60 W m<sup>-2</sup> in the northern ICP. The above BB aerosol-induced SW radiative forcing both in the  
292 atmosphere and at the surface are comparable in magnitudes to those found previously (Lin et al., 2014; Pani et al., 2018;  
293 Yang et al., 2022b).

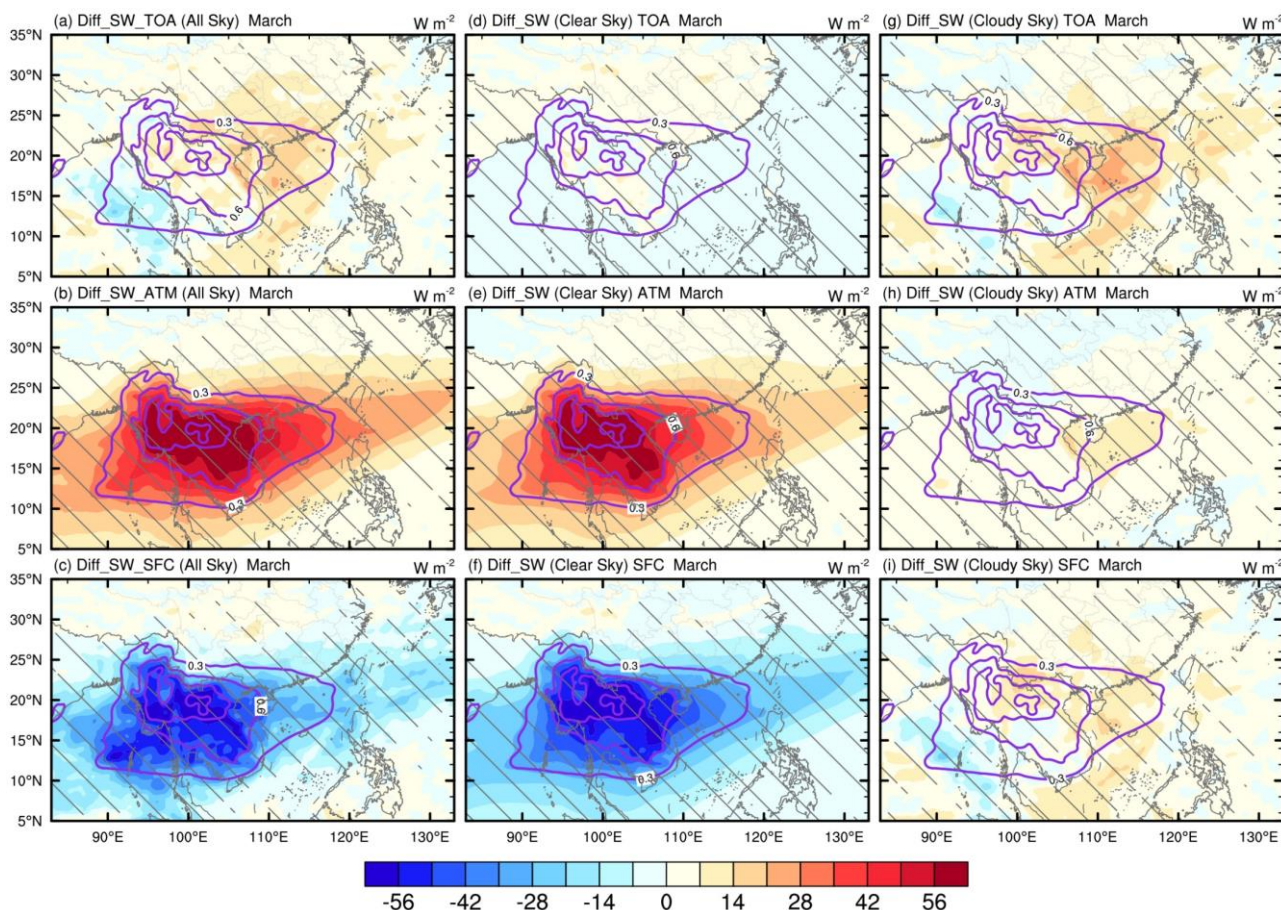
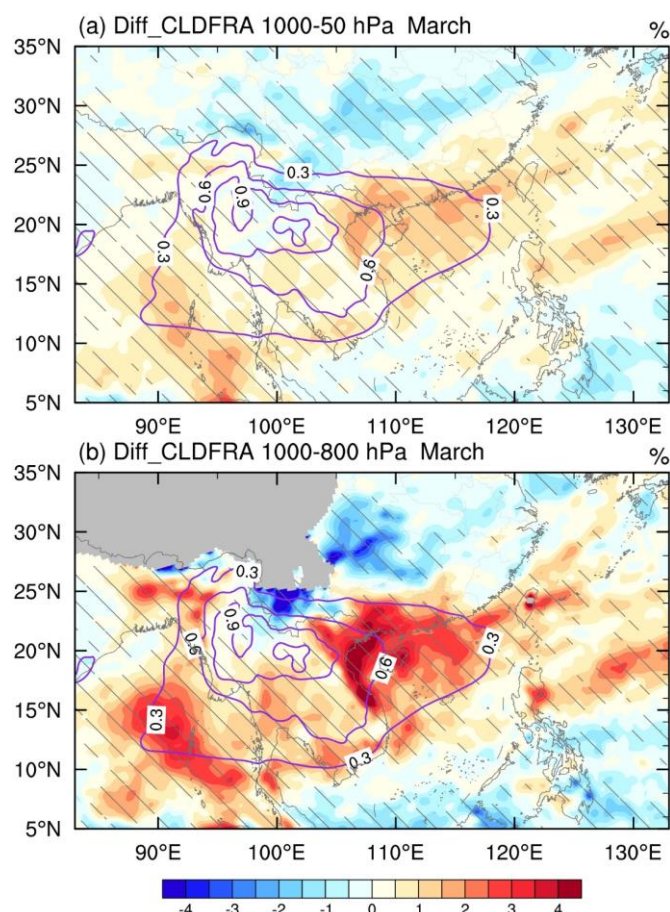


**Figure 6:** (a–c) Differences (CTRL minus BBER) in all-sky net downward shortwave radiative flux (shading;  $\text{W m}^{-2}$ ) (a) at the top of atmosphere (TOA), (b) in the atmosphere (ATM), and (c) at the surface (SFC) in March 2010. (d–f) and (g–i) Same as (a–c), but for clear-sky and cloudy-sky differences, respectively. The purple contours with interval of 0.3 denote AOD differences (CTRL minus BBER). Hatching denotes the radiative effect is statistically significant at the 95 % confidence level based on Student's  $t$ -test.

At the TOA, the positive all-sky SW radiative flux anomalies induced by BB aerosols are above  $15 \text{ W m}^{-2}$  over North Vietnam, southern China and the SCS but below  $7.5 \text{ W m}^{-2}$  over the BB emission source region in the northern ICP (Fig. 6a), which is consistent with previous results in both modeling (Lee and Kim, 2010; Dong et al., 2019) and measurement studies (Pani et al., 2016; Pani et al., 2018). Generally, BB aerosols can reflect and scatter more SW radiation back to space compared to BB aerosol-free cases, leading to a weak negative SW radiative forcing at the TOA, as demonstrated in some studies (Lee et al., 2014; Lin et al., 2014; Chavan et al., 2021; Yang et al., 2022b). Nevertheless, absorbing BB aerosols can also switch from exerting a negative to a positive SW radiative effect at the TOA, due to increased underlying cloud coverage or brightness of the underlying layer (Chand et al., 2009; Lu et al., 2018). Thus, in clear-sky conditions (i.e., radiative forcing by aerosols without the cloud-circulation feedback), the TOA SW radiative effect is negative over waters and weak positive over most of the land (Fig. 6d) due to the high surface albedo contrast between those two underlying surfaces, while the strong TOA positive radiative effect over the downstream regions of the BB aerosols' transport is mainly



310 due to the cloud-circulation feedback. Figures 6g–i show the radiative effects caused by changes in cloud fraction (measured  
 311 as the all-sky minus clear-sky radiative effects). Positive radiative effects in cloudy conditions are mostly distributed along  
 312 the coastal regions and the ocean waters off southern China and North Vietnam, with a magnitude of 14–28 W m<sup>-2</sup>. Greater  
 313 cloud covers occur in these regions (Fig. 7a), which are concentrated in the lower troposphere (i.e., 1000–800 hPa; Fig. 7b).  
 314 A previous study demonstrated that the enhancement of low clouds beneath the BB aerosol plume around 3 km over  
 315 subtropical East Asia is caused by a synergetic effect of aerosol-cloud-boundary layer interaction with the monsoon (Ding et  
 316 al., 2021). In turn, the BB aerosol plume uplifted above the clouds could absorb more solar radiation reflected from the cloud  
 317 top, thus reducing the shortwave radiation reflected back to space (Dong et al., 2019). This also means that the increasingly  
 318 thick and bright cloud layer underneath the BB aerosol plume would further amplify the direct warming effect in the  
 319 atmosphere induced by BB aerosols (Ding et al., 2021), resulting in an increase of atmospheric warming by roughly 15%–20%  
 320 (Fig. 6h). The spatial pattern of the net (LW+SW) radiative effect is dominated by the SW radiative effect, because the LW  
 321 radiative effect is relatively small. Thus, the LW and net radiative effects are not shown here.



322  
 323 **Figure 7: Differences (CTRL minus BBER) in cloud fraction (shading; %) in the (a) entire atmospheric column (1000–50 hPa) and**  
 324 **(b) lower troposphere (1000–800 hPa) in March 2010. The purple contours with interval of 0.3 denote AOD differences. Hatching**  
 325 **denotes the cloud fraction change is statistically significant at the 95 % confidence level based on Student's *t*-test.**





BB aerosols can dramatically alter the horizontal and vertical distribution of atmospheric temperatures through their radiative effects. Figure 8 shows the spatial pattern of BB aerosol-induced temperature changes from surface to 500 hPa in March 2010. Due to the surface cooling effect of BB aerosols, the surface temperature was reduced by up to 1.6K in the ICP, and the cooling could reach up to 850 hPa (Figs. 8a–b). The BB aerosol-induced warming at 700 hPa can be widely found from the Bay of Bengal across the ICP, SCS and southern China to the East China Sea, with a magnitude between 0.4 and 2.0K (Fig. 8c); and such a warming pattern generally follows the AOD anomaly pattern. As a result, the BB aerosol-induced surface cooling and 700-hPa warming acted to increase the low-level atmospheric stability. Besides, a weak atmospheric cooling effect was found in the mid troposphere (500 hPa) over the ICP (Fig. 8d).

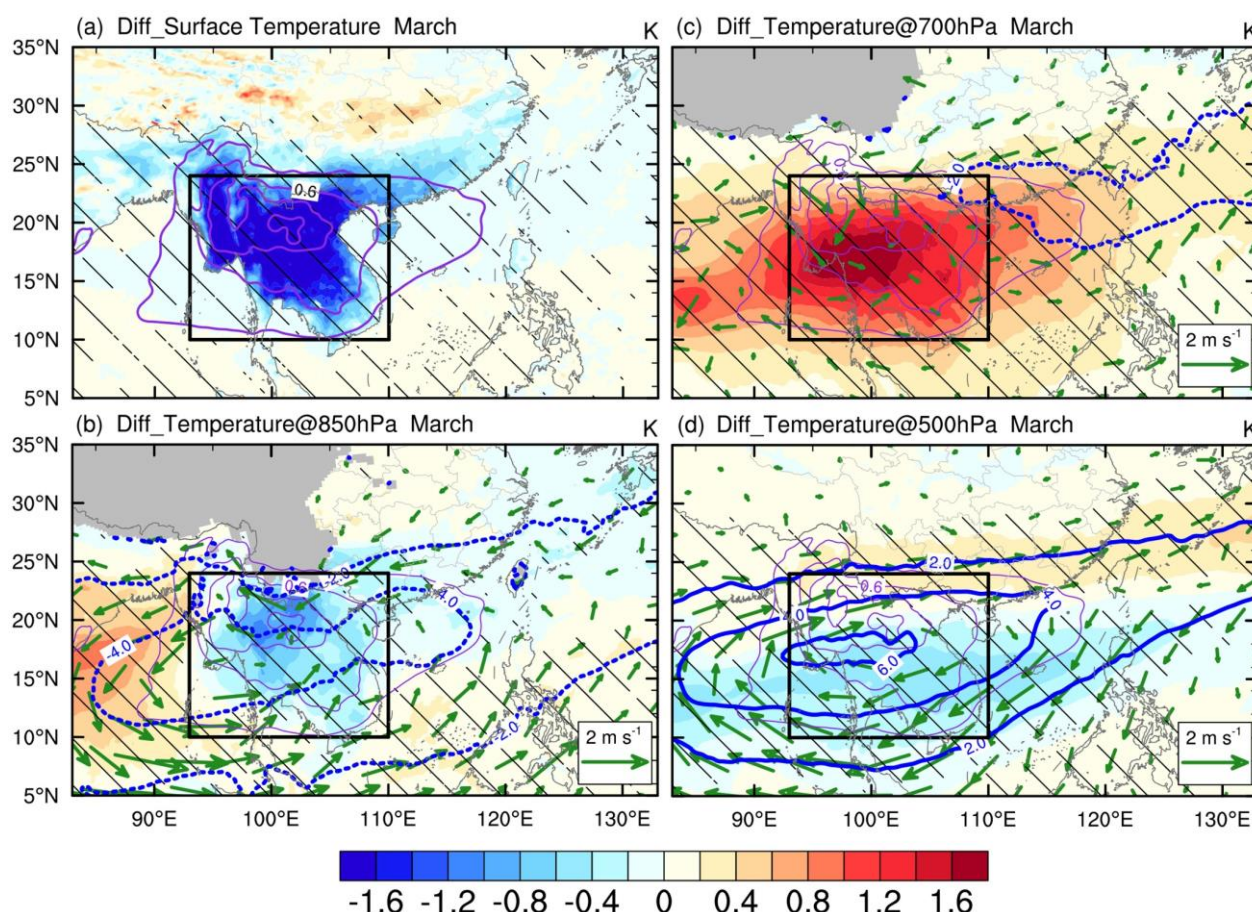


**Figure 8: Differences (CTRL minus BBER) in (a) surface temperature (shading; K), (b–d) horizontal wind (vector;  $\text{m s}^{-1}$ ), geopotential height (thick blue contours with interval of 2 dagpm; the dashed contours are for negative values and the zero contour is omitted for clarity), and temperature (shading; K) at (b) 850 hPa, (c) 700 hPa, and (d) 500 hPa in March 2010. Purple contours with interval of 0.3 denote AOD differences. The hatching and green vectors denote temperature and wind changes are statistically significant at the 95 % confidence level, respectively, based on Student's *t*-test. The black box outlines the main Indochina Peninsula (ICP; 93°–110° E, 10°–24° N).**

To better explain such “cooling-warming-cooling” vertical temperature changes from the lower to upper troposphere, we show the vertical profiles of changes in area-averaged atmospheric heating source in the ICP (93°–110° E, 10°–24° N; black



box in Fig. 8) during March (Fig. 9a). As expected, SW radiative forcing was the major factor contributing to the atmospheric heating, which was the strongest (exceeding  $1.0\text{K day}^{-1}$ ) near 650 hPa and diminished to zero near 400 hPa. Note that the height of the SW heating did not coincide with that of the BC mass concentration maximum, partially due to the amplification heating effect caused by the increased low-cloud underneath the BB smoke plume (Fig. 9b). The surface cooling caused by the solar flux reduction tends to decrease surface evapotranspiration, and reduce sensible and latent heat fluxes (Andreae et al., 2004; Feingold et al., 2005; Huang et al., 2016b). As a result, the PBL processes dominate the cooling effect in the lower troposphere (1000–700 hPa). This can also explain why the PBL cooling was weaker over the ocean than over land (Figs. 8a–b), as the surface fluxes over the ocean were much less variable (Feingold et al., 2005). The latent heat shows a weak warming effect from ~950 to 750 hPa, which can translate to promoting cloud formation by large-scale condensation and even moist convection. As shown in Figs. 7 and 9b, the increase in low clouds over the Beibu Gulf was concentrated below 850 hPa, while that over the southern ICP was at 850–750 hPa. Additionally, the latent heating also displayed a weak cooling effect at 700–500-hPa because of the reduced clouds in this layer via the cloud burn-off effect of BC (the semi-direct effect). The LW radiative forcing heating contributed to the atmospheric cooling from the surface to about 400 hPa. The net atmospheric heating (i.e., the sum of SW, LW, PBL, and latent heat), induced by BB aerosols generally exhibited a cooling effect below 850 hPa and a warming effect at 850–400 hPa. As a result, the colder temperature anomalies occurred from the surface to 800 hPa with a minimum reaching  $-0.76\text{K}$ , while warmer anomalies with a maximum greater than  $1\text{K}$  were around 800–550 hPa (Fig. 9a). These temperature anomalies can markedly increase the atmospheric stability in the lower troposphere, leading to a more unstable mid troposphere.

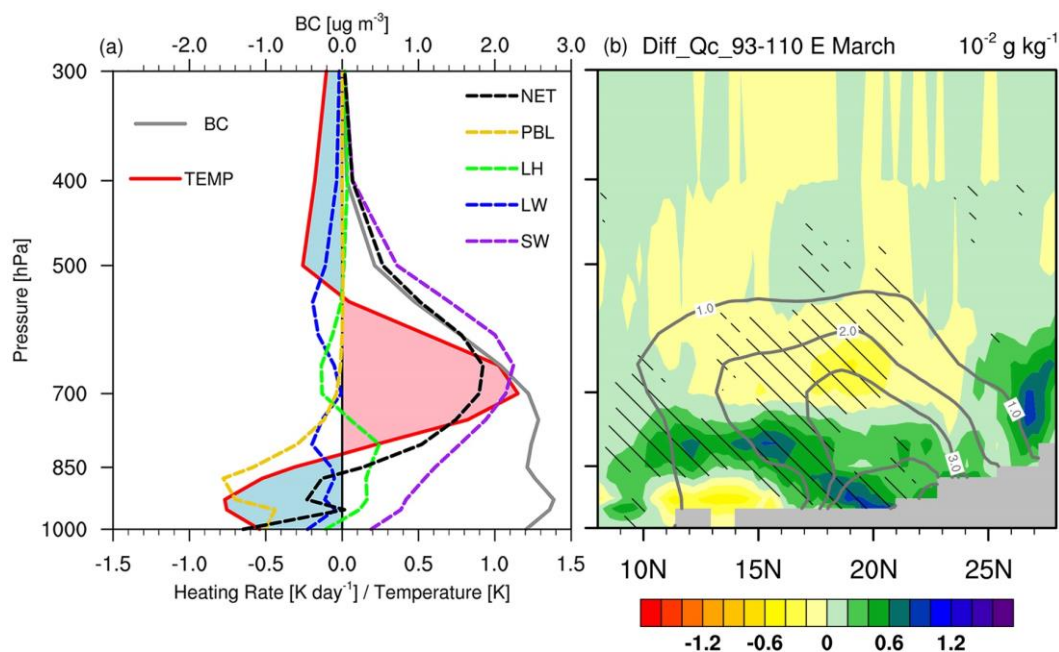


**Figure 9:** (a) Vertical profiles of differences (CTRL minus BBER) in temperature (solid red line; K), BC mass concentration (solid grey line;  $\mu\text{g m}^{-3}$ ), and atmospheric heating rates (dashed line;  $\text{K day}^{-1}$ ) averaged over ICP (93°–110° E, 10°–24° N); as outlined in Fig. 8) in March 2010. Here, atmospheric heating rates include shortwave (SW) and longwave (LW) radiation heating, latent heating





(LH; i.e., heating from microphysics and cumulus scheme), and heating from planetary boundary layer (PBL) scheme. Net heating rate (NET) = SW + LW + LH + PBL. (b) Vertical cross-sections of differences (CTRL minus BBER) in cloud water-vapor content (shading;  $10^{-2} \text{ g kg}^{-1}$ ), BC mass concentration (solid grey contours with interval of  $1.0 \text{ ug m}^{-3}$ ) averaged over  $93^{\circ}\text{--}110^{\circ}\text{E}$  in March 2010. Hatching denotes changes in cloud water-vapor content are statistically significant at the 95 % confidence level based on Student's *t*-test.

The BB aerosol-induced maximum net heating in the troposphere could reach up to  $0.9\text{K day}^{-1}$  (Fig. 9a), which was able to force anomalous atmospheric circulation. As suggested previously (Hoskins, 1991; Wu and Liu, 2000), the atmospheric response to an external diabatic heating can generate upward motion in the heating layer, cyclonic circulation in the lower atmosphere and anticyclonic circulation in the upper troposphere. These anomalous circulations can be clearly seen in our simulation results shown in Figs. 8b–d. Furthermore, subject to atmospheric thermal adaptation (Wu and Liu, 2000; Liu et al., 2001), the “overshooting” air parcel induced by the inertial ascent from below the heating layer kept a constant potential temperature, forming the cold anticyclonic circulation to the northwest of the heat source in the upper troposphere (Figs. 10a – b). Accordingly, anomalous northerly (southerly) winds across the heating region in the upper (lower) troposphere (Fig. 10a) developed to balance the Coriolis force (Liu et al., 2001). To the north of the BB aerosol heating region ( $22^{\circ}\text{--}26^{\circ}\text{N}$ ), the negative meridional diabatic heating gradient produced a negative vorticity forcing and a secondary circulation at the upper level (Figs. 10a, c). The BB aerosol-induced two-cell structure meridional circulation is quite similar to the results in Lee and Kim (2010) and Yang et al. (2022b). The sinking motion in the northern branch is consistent with the maximum precipitation anomaly in Fig. 5d. The anomalous northwesterly flow on the northern flank of the cyclonic circulation in the lower troposphere substantially weakened the water vapor transported from the Bay of Bengal to the northern ICP and southern China ( $20^{\circ}\text{--}30^{\circ}\text{N}$ ; also see Fig. 10a). However, more water vapor was lifted up from the Bay of Bengal and SCS into the mid troposphere via the Ekman pumping (Fig. 10b), which was partly transported to the central and southern ICP by anomalous southerly wind in the southern branch (Figs. 10a–b). Interestingly, precipitation was reduced in the central and southern ICP by the BB aerosols, despite of the favorable water-vapor condition (Fig. 5d). This is because the increased atmospheric stability in the low-troposphere caused by the BB aerosols greatly enhanced the convection inhibition energy (CIN) (Fig. 10d), indicative of a higher threshold for the energy required to trigger convection (Mapes, 2000). As a result, the reduction of the local convective rainfall dominated the change in precipitation over the ICP (Fig. 11a), while large-scale (stratiform) precipitation presented a minor increase (Fig. 11b). The effects of BB aerosol-induced suppression of convective precipitation and mild enhancement of large-scale precipitation over the northern ICP are consistent with the modelling results of Wang et al. (2021).

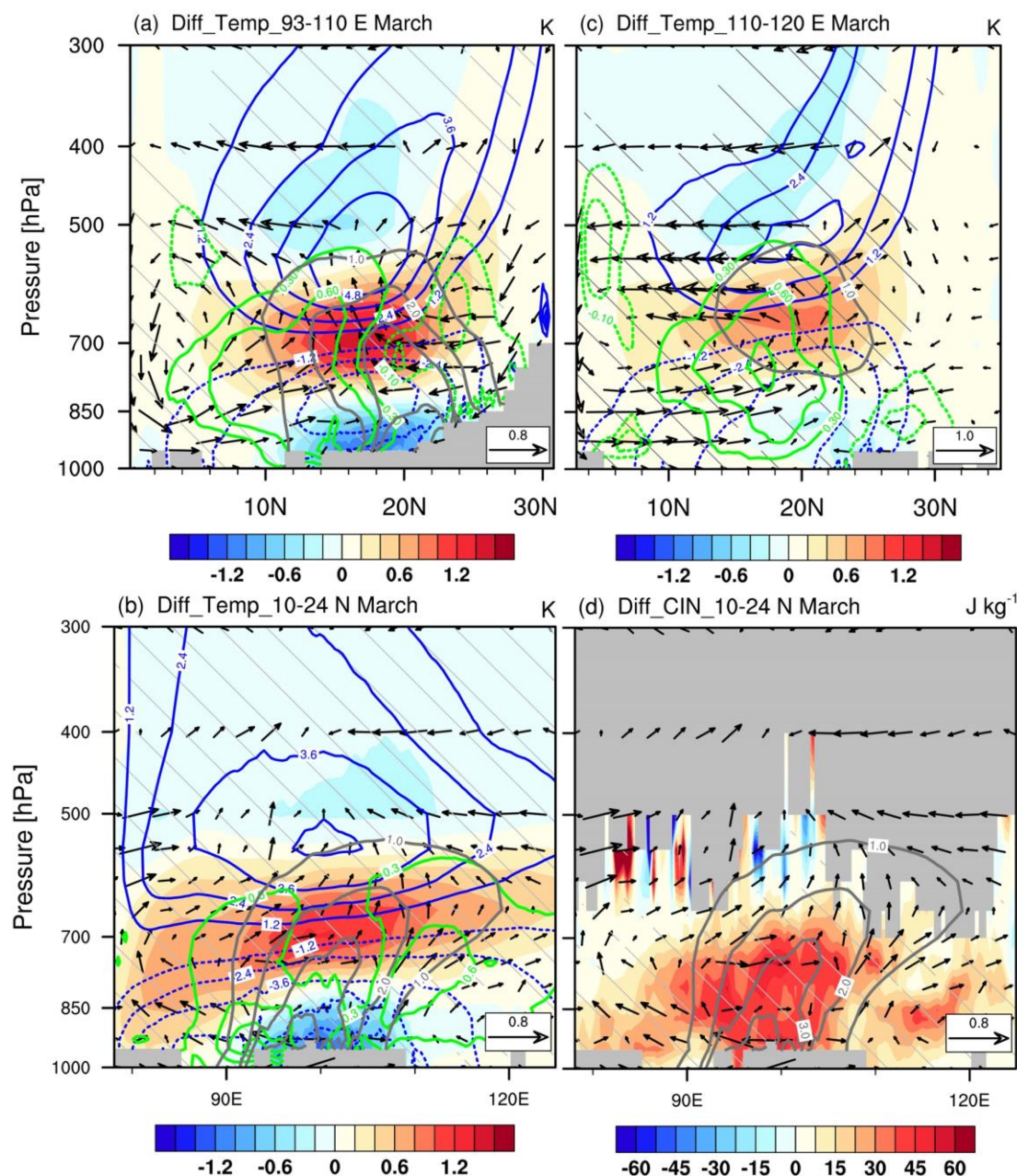
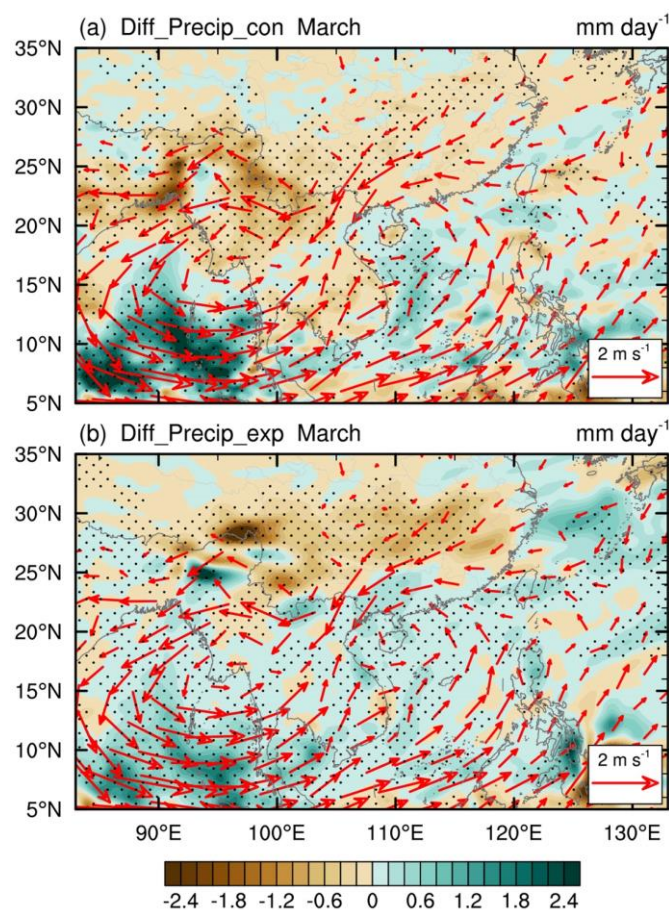


Figure 10: (a–c) Vertical cross-sections of differences (CTRL minus BBER) in temperature (shading; K), geopotential height (blue contours with interval of 1.2 dagpm; the dashed contours are for negative values and the zero contour is omitted for clarity), and water-vapor content (green contours with interval of 0.3 g kg<sup>-1</sup> for positive values and of 0.1 g kg<sup>-1</sup> for negative values, and the zero contour is omitted for clarity) averaged over (a) 93°–110° E, (b) 10°–24° N, and (c) 110°–120° E in March 2010, together with (a, c) meridional [or (b) zonal], vertical velocity (vector; m s<sup>-1</sup> and 10<sup>-2</sup> m s<sup>-1</sup>, respectively) and BC mass concentration (solid grey contours with interval of 1.0 ug m<sup>-3</sup>). (d) Same as (b), but for convective inhibition (CIN; shading; J kg<sup>-1</sup>). Hatching and vectors denote the shaded field and wind changes are statistically significant at the 95 % confidence level, respectively, based on Student's *t*-test.



**Figure 11: Differences (CTRL minus BBER) in (a) convective precipitation and (b) non-convective precipitation (shading; mm day<sup>-1</sup>) in March 2010, together with 850-hPa wind difference (vector; m s<sup>-1</sup>). Stippling and red vector denote precipitation and wind are statistically significant at the 95% confidence level, respectively, based on Student's *t*-test.**

For the SCS and its adjacent coastal water region (110 °–120 °E), the PBL cooling was quite weak (Fig. 10c), resulting in little CIN change in the lower layers (Fig. 10d). Therefore, relatively favorable water-vapor conditions led to moderately enhanced precipitation (Fig. 5d). This is similar to the “elevated heat pump” (EHP) effect proposed by Lau et al. (2006), which hypothesized that the absorbing aerosols (dust and BC) stacked up on the southern slope of the Tibetan Plateau can heat up the mid-to-upper troposphere, leading to an earlier onset of the Indian summer monsoon and increased monsoon rainfall. Note that in our case the updraft caused by the low-level (700-hPa) heating only reached 500 hPa, leading to an invigoration of shallow convection, which differs from the original “EHP” effect with a high-level (500-hPa) heating and a resultant ascent air flow reaching 200 hPa.

### 4.3.2 Delayed effect

Compared to the instant effect, the delayed effect in the subsequent April should be closely related to the atmospheric circulation adjustment, as there were a few BB aerosols left from March. During the subsequent early-April, the anomalous





vertical temperature structure still persisted with a maximum warming of 0.4K at 700 hPa and cooling of -0.6K at 925 hPa (Figs. 12a, c). Without the strong heating from the BB aerosols (Fig. 12c), the 850-hPa anomalous low over the ICP became weaker and split into a double-center system (Fig. 12b). This would increase moisture over the northern ICP and northern SCS by southerly anomalies, which facilitated precipitation over the northern ICP, southern China and the northern SCS (Figs. 12b, d and Fig. 5e).

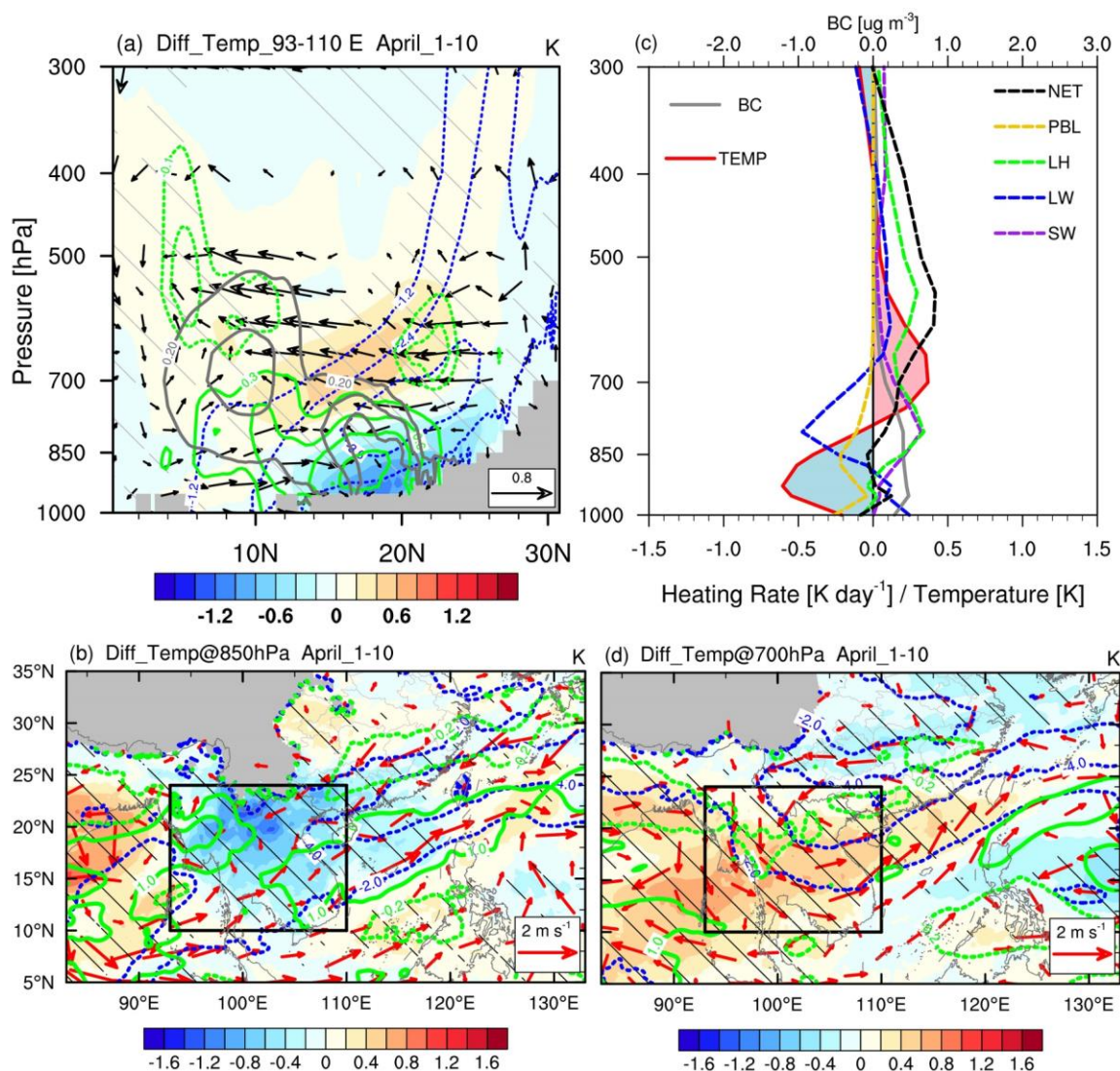
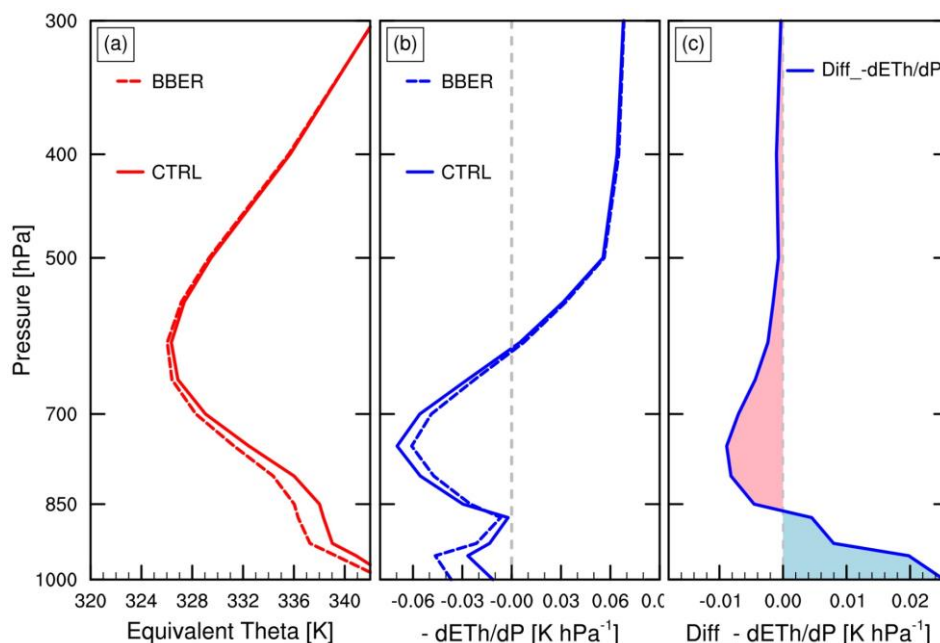


Figure 12: (a) Vertical cross-sections of differences (CTRL minus BBER) in temperature (shading; K), geopotential height (blue contours with interval of 1.2 dagpm; the dashed contours are for negative values, and the zero contour is omitted for clarity), and water-vapor content (green contours with interval of 0.3 g kg<sup>-1</sup> for positive values and of 0.1 g kg<sup>-1</sup> for negative values, and the zero contour is omitted for clarity), together with meridional and vertical velocity (vector; m s<sup>-1</sup> and 10<sup>-2</sup> m s<sup>-1</sup>, respectively) and BC mass concentration (solid grey contours with interval of 0.2 ug m<sup>-3</sup>) averaged over 93 °–110 °E. (b) Differences (CTRL minus BBER) in 850-hPa wind (vector; m s<sup>-1</sup>), geopotential height (blue contours with interval of 1.2 dagpm), water-vapor content (green contours with interval of 1.0 g kg<sup>-1</sup> for positive values and of 0.2 g kg<sup>-1</sup> for negative values, and the zero contour is omitted for



clarity), and temperature (shading; K). (c) Vertical profiles of differences (CTRL minus BBER) in temperature (solid red line; K), BC mass concentration (solid grey line;  $\mu\text{g m}^{-3}$ ), and atmospheric heating rates (dashed lines;  $\text{K day}^{-1}$ ) averaged over the ICP [black box in (b)]. (d) Same as (b), but at 700 hPa. Hatching and vector denote the shaded field and wind changes are statistically significant at the 95 % confidence level, respectively, based on Student's *t*-test. All of them are averaged over April 1<sup>st</sup>–10<sup>th</sup>, 2010 (i.e., early-April).

As analyzed in Sect. 4.3.1, the rainfall reduction over the ICP in March induced by BB aerosols resulted from competition between convection suppression by the stabilized atmosphere and favorable water vapor-conditions by large-scale circulation response. For the delayed effect in early-April, favorable water-vapor conditions due to atmospheric circulation adjustments increased significantly, as the low-level anomalous low weakened and the monsoon advanced. On the other hand, the convective instability above 850 hPa was significantly enhanced under the influence of water vapor (Fig. 13c), although the BB aerosol-induced anomalous vertical temperature structure remained. In other words, both conditions were conducive to the precipitation over the ICP in the early-April. Thus, the delayed effect acted to promote precipitation over the ICP, in contrast to inhibiting precipitation by the instant effects. In turn, the increased condensation heating associated with increased rainfall dominated the upper-air diabatic heating (Fig. 12c) via positive feedback. The adjustment in the net maximum heating layer height also led to an anomalous cyclonic circulation at 700 hPa (Fig. 12d). Due to the memory of the soil, the reduction in land surface variables such as soil temperature, soil moisture and surface evaporation can last until this period and keep the cooling effect through the PBL process (Fig. 12c). Then, all these factors acted to maintain the anomalous vertical structure of PBL cooling, upper-air warming and the anomalous circulation, so that the preceding atmospheric responses would not disappear immediately.



**Figure 13: Vertical profiles of (a) equivalent potential temperature ( $\theta_e$ ; red line; K) and (b) convective stability ( $-\frac{\partial \theta_e}{\partial p}$ ; blue line;  $\text{K hPa}^{-1}$ ) averaged over the ICP (as outlined in Fig. 12b) during April 1<sup>st</sup>–10<sup>th</sup>, 2010. The solid and dash lines are for CTRL and BBER, respectively. (c) Differences (CTRL minus BBER) in the convective stability (blue line;  $\text{K hPa}^{-1}$ ).**





Without the anomalous heating from the BB aerosols during the mid-April, the anomalous vertical temperature structure was barely seen over the ICP (Figs. 14a, c). Meanwhile, as the 850-hPa anomalous low further dissipated, anomalous southerly wind transported more water vapor from the Bay of Bengal directly northward to the northwestern ICP (Fig. 14b). The moist airflows were then lifted by the southeastern Tibetan Plateau and thus converged and cooled, which enhanced orographic precipitation (Fig. 5f). Although the BB aerosol-induced anomalous low nearly disappeared over coastal Southeast China during the mid-April, the anomalous meridional circulation accompanied by enhanced precipitation over southern China (Fig. 5f) could be sustained through the feedback from the increased condensation heating.

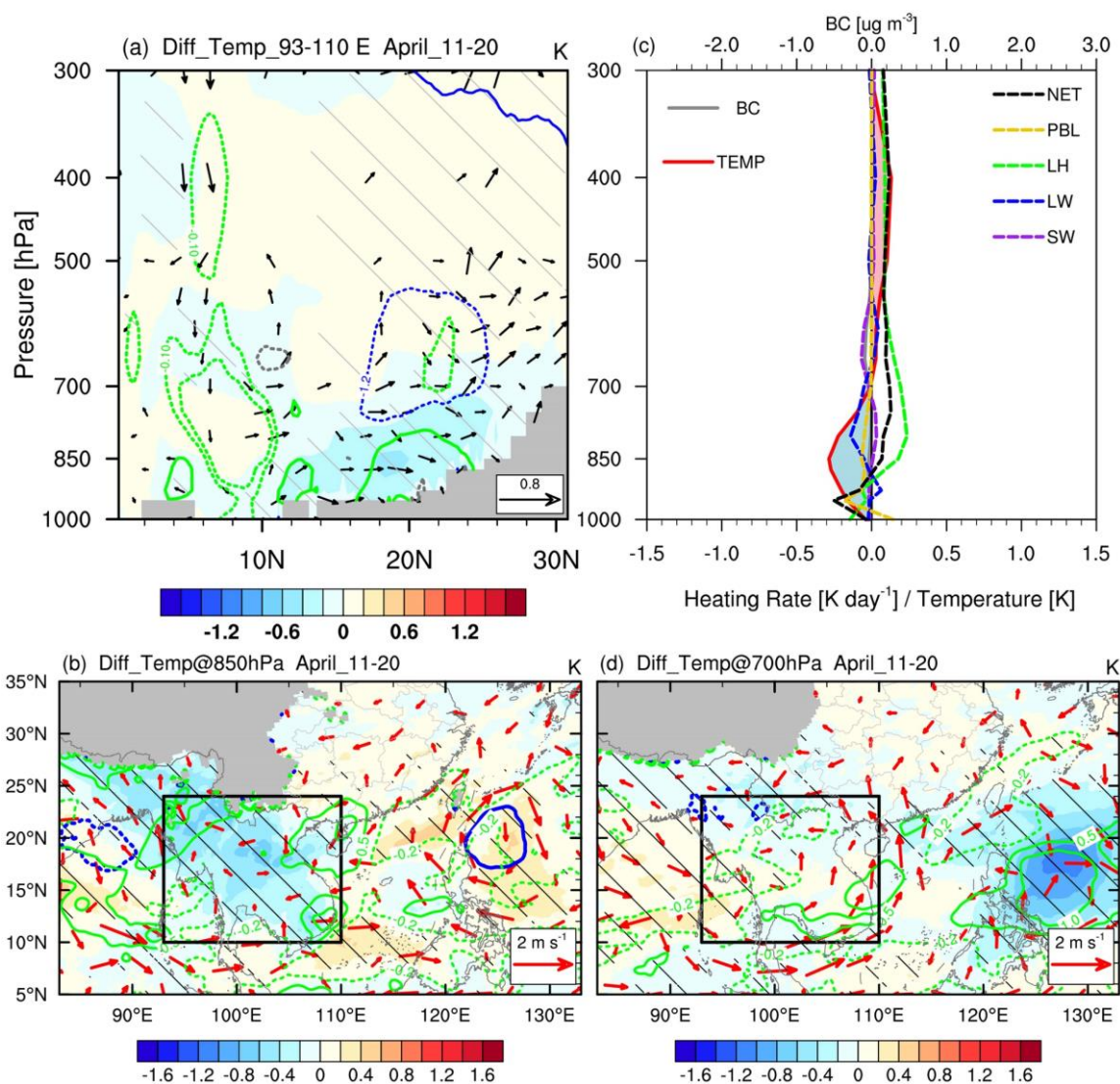


Figure 14: Same as Fig. 12, but the field are averaged over April 11<sup>th</sup>-20<sup>th</sup>, 2010 (i.e., mid-April).



## 463 5 Conclusions and discussion

464 Large amounts of absorbing aerosols are injected into the atmosphere by extensive BB activities over the ICP during March,  
465 which can significantly affect the regional climate. Using observation data and the WRF-Chem model, we investigate the  
466 instant and delayed effects of the BB aerosols over the ICP in March on the regional circulation and precipitation in early-  
467 spring. The main conclusions are summarized below.

468 The observations show that March BB aerosols are negatively correlated with the rainfall over the ICP, while such a  
469 correlation shifts to be positive in early- and mid-April, which is well captured by the WRF-Chem model. The simulation  
470 results reveal that BB aerosols emitted from the northern ICP trap a substantial proportion of solar radiation in the low-to-  
471 mid troposphere and decrease incoming solar radiation at the surface, followed by reduced surface heat fluxes associated  
472 with PBL processes. The energy perturbation leads to temperature changes in surface and lower tropospheric (1000–850-hPa)  
473 cooling and lower-to-mid tropospheric (850–400-hPa) heating. Thus, the low atmosphere is stabilized and CIN is markedly  
474 intensified at 850–700 hPa, which acts to suppress local convective rainfall. The BB aerosol-induced heating in the low-to-  
475 mid troposphere can also cause an anomalous low-pressure system in the lower troposphere extending from the central Bay  
476 of Bengal across the ICP to the northern SCS. This is accompanied by a two-cell structure meridional circulation with rising  
477 motion over the ICP and two strong downward motions in the near-equatorial regions and the latitudes of 25 °–30 °N. Over  
478 the ICP, the anomalous low in the lower troposphere tends to increase the mid-tropospheric moisture from the Bay of Bengal  
479 and SCS via moisture advection and Ekman pumping. On the southern flank of this anomalous low, the southerly wind  
480 conveys more water vapor to the ICP, causing a minor increase in large-scale precipitation. Thus, the BB aerosol-induced  
481 rainfall suppression in the ICP during March is a result of competition between the responses of local atmospheric stability  
482 and large-scale circulation to absorbing aerosols. For the SPRJ region, the anomalous northeasterly wind on the northern  
483 flank of the anomalous low would decrease the prevailing southwesterly wind and moisture transport, which is conducive to  
484 suppress the rainfall over these regions. Meanwhile, the sinking motion in the northern branch of anomalous two-cell  
485 structure meridional circulation induced by BB aerosols would also help reduce the precipitation there. Over the SCS, the  
486 moderate precipitation increase is due to favorable water-vapor conditions, while the CIN increases very little because of the  
487 insignificant PBL cooling, which is caused by the underlying water surface.

488 During early-April, the anomalous belt-shaped low-pressure weakens and fragments into a double-center system, owing to a  
489 few BB aerosols remaining in March and the corresponding reduction in BB aerosol-induced atmospheric heating. Over the  
490 ICP, although the anomalous low weakens due to lack of strong heating from the BB aerosols, it can still transport sufficient  
491 moisture from the Bay of Bengal as the monsoon advances. On the other hand, the convective instability above 850 hPa is  
492 enhanced under the influence of water vapor, although the vertical temperature anomaly structure remains. As a result, the  
493 effects of March BB aerosols on precipitation over the ICP shift from suppression in March to enhancement in early- and  
494 mid-April. In turn, the increased condensation heating associated with increased rainfall dominates the diabatic heating and  
495 sustains the anomalous circulation and vertical temperature structure via positive feedback. In mid-April, without any



anomalies directly related to BB aerosol-induced heating, the anomalous vertical temperature structure and low pressure in the lower troposphere nearly disappear, and only enhanced rainfall over the northwestern ICP and southern China can be seen due to the condensation heating.

Recently, Yang et al. (2022b) investigated the effects of BB aerosols from the ICP during the whole emission season (March 1<sup>st</sup>–April 17<sup>th</sup>, 2010). In this study, we further discuss the instant and delayed effects in the peak BB emission month of March. The instant effect of March BB aerosols on the atmospheric circulation is consistent with the results of Yang et al. (2022b). Interestingly, Yang et al. (2022b) noted that the April BB aerosols could significantly enhance the heavy rain events over the southern coast of southern China, while we show that the BB aerosol perturbation in March can induce a delayed increase in April precipitation over the same region. For the precipitation decrease over southern China, in addition to the cyclonic anomalies that reduce water vapor transport as stated by Yang et al. (2022b), we find that the sinking motion in the anomalous vertical meridional circulation induced by BB aerosol's heating also plays a role. Using an AGCM, Lee et al. (2014) suggested that the indirect effect is the main contributor to the BB aerosol-induced precipitation suppression over the ICP. In contrast, Ding et al. (2021) demonstrated that the indirect effects of BB aerosols play a less significant role in the low-cloud enhancement over subtropical Asia. Although both direct and indirect effects of aerosols are included in our experiments, we focus on the aerosol-radiation interaction (i.e., direct or semi-direct effect). The role of indirect effects needs to be investigated by setting up experiments with and without indirect effects in further.

Note that the modeling results in this study focuses only on the year of 2010, during which the AOD magnitude in March was greater than its climatology by about 1.7 standard deviations. The effects of aerosols on precipitation in the model (Figs. 5d–f) are not fully consistent with observations (Figs. 3d–f), especially for the delayed effects (Figs. 3e, f and Figs. 5e, f). Due to the fact that the response patterns of large-scale circulation and precipitation to BB aerosols largely depend on both aerosols and meteorological conditions. Thus, multiyear simulations are needed to assess the robustness of our results on a longer time scale. In addition, uncertainty may also exist in the simulation. For instance, the overestimate of convective rainfall in the tropical Bay of Bengal and orographic precipitation in the southeastern Tibetan Plateau might introduce some uncertainty in the response of large-scale circulation to BB aerosols, which is strongly related to the cumulus convection parameterization scheme and the topographic complexity (Ma and Tan, 2009; Li et al., 2022). Therefore, further experiments at convection-resolved resolution need to be conducted to reduce such uncertainty.

## **Code and Data availability.**

The source codes of WRF-Chem model are available at [https://www2.mmm.ucar.edu/wrf/users/download/get\\_source.html](https://www2.mmm.ucar.edu/wrf/users/download/get_source.html). The FNL data are available at <https://rda.ucar.edu/datasets/ds083.2/>. The BB emission data of FINN version 1.5 are available at <https://www.acom.ucar.edu/Data/fire/>. The MEIC and MIX anthropogenic emissions are available at [http://meicmodel.org/?page\\_id=541&lang=en](http://meicmodel.org/?page_id=541&lang=en). The ERA-5 Reanalysis data are available at <https://cds.climate.copernicus.eu/cdsapp#!/search?type=dataset>. MERRA-2 aerosol reanalysis data, OMI AI and TRMM



precipitation are available at <https://disc.gsfc.nasa.gov/datasets>. The MODIS AOD are available at  
[https://ladsweb.modaps.eosdis.nasa.gov/missions-and-measurements/products/MOD08\\_M3](https://ladsweb.modaps.eosdis.nasa.gov/missions-and-measurements/products/MOD08_M3). The BB emission data of  
GFEDv4 are available at [https://daac.ornl.gov/VEGETATION/guides/fire\\_emissions\\_v4\\_R1.html](https://daac.ornl.gov/VEGETATION/guides/fire_emissions_v4_R1.html).

#### Author contributions.

HX and AZ conceptualized the research goals and aims. SH and AZ ran the simulations. AZ performed the data analysis and  
visualized the results. AZ, HX, JD, and JM wrote the initial draft.

#### Acknowledgments

This work is jointly supported by the National Natural Science Foundation of China (41975106 and 42192562). We  
acknowledge the High Performance Computing Center of Nanjing University of Information Science & Technology for their  
support of this work. We also thank all the corresponding institutions for providing their data for this study.

#### Competing interests

The authors declare that they have no conflict of interest.

#### Financial support

This research has been supported by the National Natural Science Foundation of China (41975106 and 42192562).

#### References

- Adam, M. G., Tran, P. T. M., Bolan, N., and Balasubramanian, R.: Biomass burning-derived airborne particulate matter in  
Southeast Asia: A critical review, *J. Hazard. Mater.*, 407, 124760, <https://doi.org/10.1016/j.jhazmat.2020.124760>, 2021.
- Andreae, M. O., Rosenfeld, D., Artaxo, P., Costa, A. A., Frank, G. P., Longo, K. M., and Silva-Dias, M. A. F.: Smoking rain  
clouds over the Amazon, *Sci.*, 303, 1337-1342, [10.1126/science.1092779](https://doi.org/10.1126/science.1092779), 2004.
- Ban-Weiss, G. A., Cao, L., Bala, G., and Caldeira, K.: Dependence of climate forcing and response on the altitude of black  
carbon aerosols, *Clim. Dynam.*, 38, 897-911, [10.1007/s00382-011-1052-y](https://doi.org/10.1007/s00382-011-1052-y), 2012.
- Bao, Z., Wen, Z., and Wu, R.: Variability of aerosol optical depth over east Asia and its possible impacts, *J. Geophys. Res.-*  
*Atmos.*, 114, [10.1029/2008jd010603](https://doi.org/10.1029/2008jd010603), 2009.
- Bohren, C. F., and Huffman, D. R.: Absorption and scattering of light by small particles, John Wiley & Sons, New York,  
1983.



- 553 Bond, T. C., Streets, D. G., Yarber, K. F., Nelson, S. M., Woo, J.-H., and Klimont, Z.: A technology-based global inventory  
 554 of black and organic carbon emissions from combustion, *J. Geophys. Res.-Atmos.*, 109,  
 555 <https://doi.org/10.1029/2003JD003697>, 2004.
- 556 Buchard, V., Randles, C. A., Silva, A. M. d., Darmenov, A., Colarco, P. R., Govindaraju, R., Ferrare, R., Hair, J., Beyersdorf,  
 557 A. J., Ziemba, L. D., and Yu, H.: The MERRA-2 aerosol reanalysis, 1980 onward. Part II: Evaluation and case studies, *J.*  
 558 *Climate*, 30, 6851-6872, [10.1175/jcli-d-16-0613.1](https://doi.org/10.1175/jcli-d-16-0613.1), 2017.
- 559 Chand, D., Wood, R., Anderson, T. L., Satheesh, S. K., and Charlson, R. J.: Satellite-derived direct radiative effect of  
 560 aerosols dependent on cloud cover, *Nat. Geosci.*, 2, 181-184, [10.1038/ngeo437](https://doi.org/10.1038/ngeo437), 2009.
- 561 Chavan, P., Fadnavis, S., Chakroborty, T., Sioris, C. E., Griessbach, S., and Müller, R.: The outflow of Asian biomass  
 562 burning carbonaceous aerosol into the upper troposphere and lower stratosphere in spring: radiative effects seen in a global  
 563 model, *Atmos. Chem. Phys.*, 21, 14371-14384, [10.5194/acp-21-14371-2021](https://doi.org/10.5194/acp-21-14371-2021), 2021.
- 564 Chen, Y., Yang, K., Zhou, D., Qin, J., and Guo, X.: Improving the Noah land surface model in arid regions with an  
 565 appropriate parameterization of the thermal roughness length, *J. Hydrol.*, 11, 995-1006, [10.1175/2010jhm1185.1](https://doi.org/10.1175/2010jhm1185.1), 2010.
- 566 de Graaf, M., Stammes, P., Torres, O., and Koelemeijer, R. B. A.: Absorbing Aerosol Index: Sensitivity analysis, application  
 567 to GOME and comparison with TOMS, *J. Geophys. Res.-Atmos.*, 110, <https://doi.org/10.1029/2004JD005178>, 2005.
- 568 Deng, X., Tie, X., Zhou, X., Wu, D., Zhong, L., Tan, H., Li, F., Huang, X., Bi, X., and Deng, T.: Effects of Southeast Asia  
 569 biomass burning on aerosols and ozone concentrations over the Pearl River Delta (PRD) region, *Atmos. Environ.*, 42, 8493-  
 570 8501, <https://doi.org/10.1016/j.atmosenv.2008.08.013>, 2008.
- 571 Ding, K., Huang, X., Ding, A., Wang, M., Su, H., Kerminen, V.-M., Petäjä, T., Tan, Z., Wang, Z., Zhou, D., Sun, J., Liao, H.,  
 572 Wang, H., Carslaw, K., Wood, R., Zuidema, P., Rosenfeld, D., Kulmala, M., Fu, C., Pöschl, U., Cheng, Y., and Andreae, M.  
 573 O.: Aerosol-boundary-layer-monsoon interactions amplify semi-direct effect of biomass smoke on low cloud formation in  
 574 Southeast Asia, *Nat. Commun.*, 12, 6416, [10.1038/s41467-021-26728-4](https://doi.org/10.1038/s41467-021-26728-4), 2021.
- 575 Dong, X., Fu, J. S., Huang, K., Zhu, Q., and Tipton, M.: Regional climate effects of biomass burning and dust in East Asia:  
 576 Evidence from modeling and observation, *Geophys. Res. Lett.*, 46, 11490-11499, [10.1029/2019gl083894](https://doi.org/10.1029/2019gl083894), 2019.
- 577 Feingold, G., Jiang, H., and Harrington, J. Y.: On smoke suppression of clouds in Amazonia, *Geophys. Res. Lett.*, 32,  
 578 <https://doi.org/10.1029/2004GL021369>, 2005.
- 579 Gautam, R., Hsu, N. C., Eck, T. F., Holben, B. N., Janjai, S., Jantarach, T., Tsay, S.-C., and Lau, W. K.: Characterization of  
 580 aerosols over the Indochina peninsula from satellite-surface observations during biomass burning pre-monsoon season,  
 581 *Atmos. Environ.*, 78, 51-59, <https://doi.org/10.1016/j.atmosenv.2012.05.038>, 2013.
- 582 Gelaro, R., McCarty, W., Suárez, M. J., Todling, R., Molod, A., Takacs, L., Randles, C. A., Darmenov, A., Bosilovich, M.  
 583 G., Reichle, R., Wargan, K., Coy, L., Cullather, R., Draper, C., Akella, S., Buchard, V., Conaty, A., da Silva, A. M., Gu, W.,  
 584 Kim, G.-K., Koster, R., Lucchesi, R., Merkova, D., Nielsen, J. E., Partyka, G., Pawson, S., Putman, W., Rienecker, M.,  
 585 Schubert, S. D., Sienkiewicz, M., and Zhao, B.: The modern-era retrospective analysis for research and applications, version  
 586 2 (MERRA-2), *J. Climate*, 30, 5419-5454, [10.1175/jcli-d-16-0758.1](https://doi.org/10.1175/jcli-d-16-0758.1), 2017.





- 587 Gonçalves, W. A., Machado, L. A. T., and Kirstetter, P. E.: Influence of biomass aerosol on precipitation over the Central  
 588 Amazon: an observational study, *Atmos. Chem. Phys.*, 15, 6789-6800, 10.5194/acp-15-6789-2015, 2015.
- 589 Grell, G. A., and Freitas, S. R.: A scale and aerosol aware stochastic convective parameterization for weather and air quality  
 590 modeling, *Atmos. Chem. Phys.*, 14, 5233-5250, 10.5194/acp-14-5233-2014, 2014.
- 591 Guenther, A. B., Jiang, X., Heald, C. L., Sakulyanontvittaya, T., Duhl, T., Emmons, L. K., and Wang, X.: The model of  
 592 emissions of gases and aerosols from nature version 2.1 (MEGAN2.1): an extended and updated framework for modeling  
 593 biogenic emissions, *Geosci. Model Dev.*, 5, 1471-1492, 10.5194/gmd-5-1471-2012, 2012.
- 594 Gupta, P., Levy, R. C., Mattoo, S., Remer, L. A., and Munchak, L. A.: A surface reflectance scheme for retrieving aerosol  
 595 optical depth over urban surfaces in MODIS Dark Target retrieval algorithm, *Atmos. Meas. Tech.*, 9, 3293-3308,  
 596 10.5194/amt-9-3293-2016, 2016.
- 597 Heidinger, A. K., Foster, M. J., Walther, A., and Zhao, X.: The pathfinder atmospheres–extended AVHRR climate dataset, *B.*  
 598 *Am. Meteorol. Soc.*, 95, 909-922, 10.1175/bams-d-12-00246.1, 2014.
- 599 Herbert, R., Stier, P., and Dagan, G.: Isolating large-scale smoke impacts on cloud and precipitation processes over the  
 600 Amazon with convection permitting resolution, *J. Geophys. Res.-Atmos.*, 126, e2021JD034615,  
 601 <https://doi.org/10.1029/2021JD034615>, 2021.
- 602 Hersbach, H., and Dee, D.: ERA5 reanalysis is in production, *ECMWF newsletter*, 147, 5-6, 2016.
- 603 Hodnebrog, Ø., Myhre, G., Forster, P. M., Sillmann, J., and Samset, B. H.: Local biomass burning is a dominant cause of the  
 604 observed precipitation reduction in southern Africa, *Nat. Commun.*, 7, 11236, 10.1038/ncomms11236, 2016.
- 605 Holben, B. N., Eck, T. F., Slutsker, I., Tanré, D., Buis, J. P., Setzer, A., Vermote, E., Reagan, J. A., Kaufman, Y. J.,  
 606 Nakajima, T., Lavenue, F., Jankowiak, I., and Smirnov, A.: AERONET—A federated instrument network and data archive  
 607 for aerosol characterization, *Remote. Sens. Environ.*, 66, 1-16, [https://doi.org/10.1016/S0034-4257\(98\)00031-5](https://doi.org/10.1016/S0034-4257(98)00031-5), 1998.
- 608 Hoskins, B. J.: Towards a PV- $\theta$  view of the general circulation, *Tellus A*, 43, 27-36, 10.3402/tellusa.v43i4.11936, 1991.
- 609 Huang, H.-Y., Wang, S.-H., Huang, W.-X., Lin, N.-H., Chuang, M.-T., da Silva, A. M., and Peng, C.-M.: Influence of  
 610 synoptic-dynamic meteorology on the long-range transport of Indochina biomass burning aerosols, *J. Geophys. Res.-Atmos.*,  
 611 125, e2019JD031260, <https://doi.org/10.1029/2019JD031260>, 2020.
- 612 Huang, K., Fu, J. S., Hsu, N. C., Gao, Y., Dong, X., Tsay, S.-C., and Lam, Y. F.: Impact assessment of biomass burning on  
 613 air quality in Southeast and East Asia during BASE-ASIA, *Atmos. Environ.*, 78, 291-302,  
 614 <https://doi.org/10.1016/j.atmosenv.2012.03.048>, 2013.
- 615 Huang, W.-R., Wang, S.-H., Yen, M.-C., Lin, N.-H., and Promchote, P.: Interannual variation of springtime biomass burning  
 616 in Indochina: Regional differences, associated atmospheric dynamical changes, and downwind impacts, *J. Geophys. Res.-*  
 617 *Atmos.*, 121, 10,016-010,028, 10.1002/2016jd025286, 2016a.
- 618 Huang, X., Ding, A., Liu, L., Liu, Q., Ding, K., Niu, X., Nie, W., Xu, Z., Chi, X., Wang, M., Sun, J., Guo, W., and Fu, C.:  
 619 Effects of aerosol–radiation interaction on precipitation during biomass-burning season in East China, *Atmos. Chem. Phys.*,  
 620 16, 10063-10082, 10.5194/acp-16-10063-2016, 2016b.



- 621 Huffman, G. J., Bolvin, D. T., Nelkin, E. J., Wolff, D. B., Adler, R. F., Gu, G., Hong, Y., Bowman, K. P., and Stocker, E. F.:  
 622 The TRMM multisatellite precipitation analysis (TMPA): Quasi-global, multiyear, combined-sensor precipitation estimates  
 623 at fine scales, *J. Hydrol.*, 8, 38-55, 10.1175/jhm560.1, 2007.
- 624 Iacono, M. J., Delamere, J. S., Mlawer, E. J., Shephard, M. W., Clough, S. A., and Collins, W. D.: Radiative forcing by long-  
 625 lived greenhouse gases: Calculations with the AER radiative transfer models, *J. Geophys. Res.-Atmos.*, 113,  
 626 <https://doi.org/10.1029/2008JD009944>, 2008.
- 627 Jacobson, M. Z.: Effects of biomass burning on climate, accounting for heat and moisture fluxes, black and brown carbon,  
 628 and cloud absorption effects, *J. Geophys. Res.-Atmos.*, 119, 8980-9002, <https://doi.org/10.1002/2014JD021861>, 2014.
- 629 Janjić, Z. I.: The step-mountain eta coordinate model: Further developments of the convection, viscous sublayer, and  
 630 turbulence closure schemes, *Mon. Weather Rev.*, 122, 927-945, 10.1175/1520-0493(1994)122<0927:tsmecm>2.0.co;2, 1994.
- 631 Jiang, Y., Yang, X.-Q., Liu, X., Qian, Y., Zhang, K., Wang, M., Li, F., Wang, Y., and Lu, Z.: Impacts of wildfire aerosols on  
 632 global energy budget and climate: The role of climate feedbacks, *J. Climate*, 33, 3351-3366, 10.1175/jcli-d-19-0572.1, 2020.
- 633 Kahn, R. A., Gaitley, B. J., Martonchik, J. V., Diner, D. J., Crean, K. A., and Holben, B.: Multiangle Imaging  
 634 Spectroradiometer (MISR) global aerosol optical depth validation based on 2 years of coincident Aerosol Robotic Network  
 635 (AERONET) observations, *J. Geophys. Res.-Atmos.*, 110, <https://doi.org/10.1029/2004JD004706>, 2005.
- 636 Kaskaoutis, D. G., Nastos, P. T., Kosmopoulos, P. G., Kambezidis, H. D., Kharol, S. K., and Badarinath, K. V. S.: The  
 637 Aura-OMI Aerosol Index distribution over Greece, *Atmos. Res.*, 98, 28-39, <https://doi.org/10.1016/j.atmosres.2010.03.018>,  
 638 2010.
- 639 Koren, I., Kaufman, Y. J., Remer, L. A., and Martins, J. V.: Measurement of the effect of Amazon smoke on inhibition of  
 640 cloud formation, *Science*, 303, 1342-1345, 10.1126/science.1089424, 2004.
- 641 Lau, K. M., Kim, M. K., and Kim, K. M.: Asian summer monsoon anomalies induced by aerosol direct forcing: the role of  
 642 the Tibetan Plateau, *Clim. Dynam.*, 26, 855-864, 10.1007/s00382-006-0114-z, 2006.
- 643 Lau, W. K. M.: The aerosol-monsoon climate system of Asia: A new paradigm, *J. Meteorol. Res.-PRC.*, 30, 1-11,  
 644 10.1007/s13351-015-5999-1, 2016.
- 645 Lee, D., Sud, Y. C., Oreopoulos, L., Kim, K. M., Lau, W. K., and Kang, I. S.: Modeling the influences of aerosols on pre-  
 646 monsoon circulation and rainfall over Southeast Asia, *Atmos. Chem. Phys.*, 14, 6853-6866, 10.5194/acp-14-6853-2014,  
 647 2014.
- 648 Lee, H. H., and Wang, C.: The impacts of biomass burning activities on convective systems over the Maritime Continent,  
 649 *Atmos. Chem. Phys.*, 20, 2533-2548, 10.5194/acp-20-2533-2020, 2020.
- 650 Lee, W.-S., and Kim, M.-K.: Effects of radiative forcing by black carbon aerosol on spring rainfall decrease over Southeast  
 651 Asia, *Atmos. Environ.*, 44, 3739-3744, <https://doi.org/10.1016/j.atmosenv.2010.06.058>, 2010.
- 652 LeGrand, S. L., Polashenski, C., Letcher, T. W., Creighton, G. A., Peckham, S. E., and Cetola, J. D.: The AFWA dust  
 653 emission scheme for the GOCART aerosol model in WRF-Chem v3.8.1, *Geosci. Model Dev.*, 12, 131-166, 10.5194/gmd-  
 654 12-131-2019, 2019.



- 655 Levy, R. C., Remer, L. A., Kleidman, R. G., Mattoo, S., Ichoku, C., Kahn, R., and Eck, T. F.: Global evaluation of the  
 656 Collection 5 MODIS dark-target aerosol products over land, *Atmos. Chem. Phys.*, 10, 10399-10420, 10.5194/acp-10-10399-  
 657 2010, 2010.
- 658 Li, G., Chen, H., Xu, M., Zhao, C., Zhong, L., Li, R., Fu, Y., and Gao, Y.: Impacts of topographic complexity on modeling  
 659 moisture transport and precipitation over the Tibetan Plateau in summer, *Adv. Atmos. Sci.*, 10.1007/s00376-022-1409-7,  
 660 2022.
- 661 Li, M., Liu, H., Geng, G., Hong, C., Liu, F., Song, Y., Tong, D., Zheng, B., Cui, H., Man, H., Zhang, Q., and He, K.:  
 662 Anthropogenic emission inventories in China: a review, *Natl. Sci. Rev.*, 4, 834-866, 10.1093/nsr/nwx150, 2017a.
- 663 Li, M., Zhang, Q., Kurokawa, J. I., Woo, J. H., He, K., Lu, Z., Ohara, T., Song, Y., Streets, D. G., Carmichael, G. R., Cheng,  
 664 Y., Hong, C., Huo, H., Jiang, X., Kang, S., Liu, F., Su, H., and Zheng, B.: MIX: a mosaic Asian anthropogenic emission  
 665 inventory under the international collaboration framework of the MICS-Asia and HTAP, *Atmos. Chem. Phys.*, 17, 935-963,  
 666 10.5194/acp-17-935-2017, 2017b.
- 667 Li, Z., Lau, W. K.-M., Ramanathan, V., Wu, G., Ding, Y., Manoj, M. G., Liu, J., Qian, Y., Li, J., Zhou, T., Fan, J., Rosenfeld,  
 668 D., Ming, Y., Wang, Y., Huang, J., Wang, B., Xu, X., Lee, S.-S., Cribb, M., Zhang, F., Yang, X., Zhao, C., Takemura, T.,  
 669 Wang, K., Xia, X., Yin, Y., Zhang, H., Guo, J., Zhai, P. M., Sugimoto, N., Babu, S. S., and Brasseur, G. P.: Aerosol and  
 670 monsoon climate interactions over Asia, *Rev. Geophys.*, 54, 866-929, <https://doi.org/10.1002/2015RG000500>, 2016.
- 671 Lin, C.-Y., Zhao, C., Liu, X., Lin, N.-H., and Chen, W.-N.: Modelling of long-range transport of Southeast Asia biomass-  
 672 burning aerosols to Taiwan and their radiative forcings over East Asia, *Tellus B*, 66, 23733, 10.3402/tellusb.v66.23733, 2014.
- 673 Lin, C. Y., Hsu, H. m., Lee, Y. H., Kuo, C. H., Sheng, Y. F., and Chu, D. A.: A new transport mechanism of biomass  
 674 burning from Indochina as identified by modeling studies, *Atmos. Chem. Phys.*, 9, 7901-7911, 10.5194/acp-9-7901-2009,  
 675 2009.
- 676 Liu, L., Cheng, Y., Wang, S., Wei, C., Pöhlker, M. L., Pöhlker, C., Artaxo, P., Shrivastava, M., Andreae, M. O., Pöschl, U.,  
 677 and Su, H.: Impact of biomass burning aerosols on radiation, clouds, and precipitation over the Amazon: relative importance  
 678 of aerosol–cloud and aerosol–radiation interactions, *Atmos. Chem. Phys.*, 20, 13283-13301, 10.5194/acp-20-13283-2020,  
 679 2020.
- 680 Liu, Y., Wu, G., Yu, R., and Liu, X.: Thermal adaptation, overshooting, dispersion, and subtropical anticyclone part II:  
 681 Horizontal inhomogeneous heating and energy dispersion, *Chinese J. of Atmos. Sci. (in Chinese)*, 25, 317-328,  
 682 10.3878/j.issn.1006-9895.2001.03.03, 2001.
- 683 Lu, Z., Liu, X., Zhang, Z., Zhao, C., Meyer, K., Rajapakshe, C., Wu, C., Yang, Z., and Penner, J. E.: Biomass smoke from  
 684 southern Africa can significantly enhance the brightness of stratocumulus over the southeastern Atlantic Ocean, *P. Natl.*  
 685 *Acad. Sci. USA*, 115, 2924-2929, 10.1073/pnas.1713703115, 2018.
- 686 Ma, L.-M., and Tan, Z.-M.: Improving the behavior of the cumulus parameterization for tropical cyclone prediction:  
 687 Convection trigger, *Atmos. Res.*, 92, 190-211, <https://doi.org/10.1016/j.atmosres.2008.09.022>, 2009.





- 688 Mapes, B. E.: Convective inhibition, subgrid-scale triggering energy, and stratiform instability in a toy tropical wave model,  
 689 J. Atmos. Sci., 57, 1515-1535, 10.1175/1520-0469(2000)057<1515:cisste>2.0.co;2, 2000.
- 690 Martins, J. A., Silva Dias, M. A. F., and Gonçalves, F. L. T.: Impact of biomass burning aerosols on precipitation in the  
 691 Amazon: A modeling case study, J. Geophys. Res.-Atmos., 114, <https://doi.org/10.1029/2007JD009587>, 2009.
- 692 Morrison, H., Thompson, G., and Tatarskii, V.: Impact of cloud microphysics on the development of trailing stratiform  
 693 precipitation in a simulated squall line: Comparison of one- and two-moment schemes, Mon. Weather Rev., 137, 991-1007,  
 694 10.1175/2008mwr2556.1, 2009.
- 695 Myhre, G., Stordal, F., Johnsrud, M., Kaufman, Y. J., Rosenfeld, D., Storelvmo, T., Kristjansson, J. E., Berntsen, T. K.,  
 696 Myhre, A., and Isaksen, I. S. A.: Aerosol-cloud interaction inferred from MODIS satellite data and global aerosol models,  
 697 Atmos. Chem. Phys., 7, 3081-3101, 10.5194/acp-7-3081-2007, 2007.
- 698 Ning, G., Wang, S., Ma, M., Ni, C., Shang, Z., Wang, J., and Li, J.: Characteristics of air pollution in different zones of  
 699 Sichuan Basin, China, Sci. Total Environ., 612, 975-984, <https://doi.org/10.1016/j.scitotenv.2017.08.205>, 2018.
- 700 Pahlow, M., Parlange, M. B., and Porté-Agel, F.: On Monin–Obukhov similarity in the stable atmospheric boundary layer,  
 701 Bound.-Lay. Meteorol., 99, 225-248, 10.1023/A:1018909000098, 2001.
- 702 Pani, S. K., Wang, S.-H., Lin, N.-H., Lee, C.-T., Tsay, S.-C., Holben, B. N., Janjai, S., Hsiao, T.-C., Chuang, M.-T., and  
 703 Chantara, S.: Radiative effect of springtime biomass-burning aerosols over northern Indochina during 7-SEAS/BASELInE  
 704 2013 campaign, Aerosol Air Qual. Res., 16, 2802-2817, 10.4209/aaqr.2016.03.0130, 2016.
- 705 Pani, S. K., Lin, N.-H., Chantara, S., Wang, S.-H., Khamkaew, C., Prapamontol, T., and Janjai, S.: Radiative response of  
 706 biomass-burning aerosols over an urban atmosphere in northern peninsular Southeast Asia, Sci. Total Environ., 633, 892-911,  
 707 <https://doi.org/10.1016/j.scitotenv.2018.03.204>, 2018.
- 708 Qin, Y., and Xie, S. D.: Spatial and temporal variation of anthropogenic black carbon emissions in China for the period  
 709 1980–2009, Atmos. Chem. Phys., 12, 4825-4841, 10.5194/acp-12-4825-2012, 2012.
- 710 Randerson, J. T., Van Der Werf, G. R., Giglio, L., Collatz, G. J., and Kasibhatla, P. S.: Global fire emissions database,  
 711 version 4.1 (GFEDv4), ORNL Distributed Active Archive Center, 2017.
- 712 Reid, J. S., Koppmann, R., Eck, T. F., and Eleuterio, D. P.: A review of biomass burning emissions part II: intensive physical  
 713 properties of biomass burning particles, Atmos. Chem. Phys., 5, 799-825, 10.5194/acp-5-799-2005, 2005.
- 714 Requia, W. J., Amini, H., Mukherjee, R., Gold, D. R., and Schwartz, J. D.: Health impacts of wildfire-related air pollution in  
 715 Brazil: a nationwide study of more than 2 million hospital admissions between 2008 and 2018, Nat. Commun., 12, 6555,  
 716 10.1038/s41467-021-26822-7, 2021.
- 717 Sakaeda, N., Wood, R., and Rasch, P. J.: Direct and semidirect aerosol effects of southern African biomass burning aerosol,  
 718 J. Geophys. Res.-Atmos., 116, <https://doi.org/10.1029/2010JD015540>, 2011.
- 719 Shi, Y., Sasai, T., and Yamaguchi, Y.: Spatio-temporal evaluation of carbon emissions from biomass burning in Southeast  
 720 Asia during the period 2001–2010, Ecol. Model., 272, 98-115, <https://doi.org/10.1016/j.ecolmodel.2013.09.021>, 2014.



- 721 Torres, O., Tanskanen, A., Veihelmann, B., Ahn, C., Braak, R., Bhartia, P. K., Veefkind, P., and Levelt, P.: Aerosols and  
 722 surface UV products from Ozone Monitoring Instrument observations: An overview, *J. Geophys. Res.-Atmos.*, 112,  
 723 <https://doi.org/10.1029/2007JD008809>, 2007.
- 724 Tummon, F., Solmon, F., Liou, S. C., and Tadross, M.: Simulation of the direct and semidirect aerosol effects on the  
 725 southern Africa regional climate during the biomass burning season, *J. Geophys. Res.-Atmos.*, 115,  
 726 <https://doi.org/10.1029/2009JD013738>, 2010.
- 727 Wang, J., Jiang, Q., You, Y., Rao, X., Sheng, L., Gui, H., Hua, C., and Zhang, B.: Effects of biomass burning aerosol in  
 728 Southeast Asia on haze and precipitation over China, *Meteor. Mon.* (in Chinese), 47, 348-358, 2021.
- 729 Wiedinmyer, C., Akagi, S. K., Yokelson, R. J., Emmons, L. K., Al-Saadi, J. A., Orlando, J. J., and Soja, A. J.: The Fire  
 730 INventory from NCAR (FINN): a high resolution global model to estimate the emissions from open burning, *Geosci. Model*  
 731 *Dev.*, 4, 625-641, [10.5194/gmd-4-625-2011](https://doi.org/10.5194/gmd-4-625-2011), 2011.
- 732 Wu, G., and Liu, Y.: Thermal adaptation, overshooting, dispersion, and subtropical anticyclone part I: Thermal adaptation  
 733 and overshooting, *Chinese J. of Atmos. Sci.* (in Chinese), 24, 433-446, [10.3878/j.issn.1006-9895.2000.04.01](https://doi.org/10.3878/j.issn.1006-9895.2000.04.01) 2000.
- 734 Wu, G., Li, Z., Fu, C., Zhang, X., Zhang, R., Zhang, R., Zhou, T., Li, J., Li, J., Zhou, D., Wu, L., Zhou, L., He, B., and  
 735 Huang, R.: Advances in studying interactions between aerosols and monsoon in China, *Sci. China Earth Sci.*, 59, 1-16,  
 736 [10.1007/s11430-015-5198-z](https://doi.org/10.1007/s11430-015-5198-z), 2016.
- 737 Yadav, I. C., Linthoingambi Devi, N., Li, J., Syed, J. H., Zhang, G., and Watanabe, H.: Biomass burning in Indo-China  
 738 peninsula and its impacts on regional air quality and global climate change-a review, *Environ. Pollut.*, 227, 414-427,  
 739 <https://doi.org/10.1016/j.envpol.2017.04.085>, 2017.
- 740 Yang, Q., Zhao, T., Tian, Z., Kumar, K. R., Chang, J., Hu, W., Shu, Z., and Hu, J.: The cross-border transport of PM<sub>2.5</sub> from  
 741 the Southeast Asian biomass burning emissions and its impact on air pollution in Yunnan Plateau, Southwest China, *Remote*  
 742 *Sens.-Basel*, 14, 1886, 2022a.
- 743 Yang, S., Lau, W. K. M., Ji, Z., Dong, W., and Yang, S.: Impacts of radiative effect of pre-monsoon biomass burning  
 744 aerosols on atmospheric circulation and rainfall over Southeast Asia and southern China, *Clim. Dynam.*, [10.1007/s00382-](https://doi.org/10.1007/s00382-021-06135-7)  
 745 [021-06135-7](https://doi.org/10.1007/s00382-021-06135-7), 2022b.
- 746 Zaveri, R. A., and Peters, L. K.: A new lumped structure photochemical mechanism for large-scale applications, *J. Geophys.*  
 747 *Res.-Atmos.*, 104, 30387-30415, <https://doi.org/10.1029/1999JD900876>, 1999.
- 748 Zaveri, R. A., Easter, R. C., Fast, J. D., and Peters, L. K.: Model for simulating aerosol interactions and chemistry  
 749 (MOSAIC), *J. Geophys. Res.-Atmos.*, 113, <https://doi.org/10.1029/2007JD008782>, 2008.
- 750 Zhang, Y., Fu, R., Yu, H., Qian, Y., Dickinson, R., Silva Dias, M. A. F., da Silva Dias, P. L., and Fernandes, K.: Impact of  
 751 biomass burning aerosol on the monsoon circulation transition over Amazonia, *Geophys. Res. Lett.*, 36,  
 752 <https://doi.org/10.1029/2009GL037180>, 2009.



753 Zhao, J., Ma, X., Wu, S., and Sha, T.: Dust emission and transport in Northwest China: WRF-Chem simulation and  
754 comparisons with multi-sensor observations, *Atmos. Res.*, 241, 104978, <https://doi.org/10.1016/j.atmosres.2020.104978>,  
755 2020.

756 Zhou, Y., Yan, H., and Luo, J.-J.: Impacts of amazon fire aerosols on the subseasonal circulations of the mid-high latitudes,  
757 *Front. Earth Sci.*, 8, 10.3389/feart.2020.609554, 2021.

758 Zhu, A., Xu, H., Deng, J., Ma, J., and Li, S.: El Niño–Southern Oscillation (ENSO) effect on interannual variability in spring  
759 aerosols over East Asia, *Atmos. Chem. Phys.*, 21, 5919–5933, 10.5194/acp-21-5919-2021, 2021.

760